Utrecht University

Bi(111): A New Quantum Simulation Platform?

Improving Energy Resolution & Introducing Spin-Orbit Coupling

Author
Jan P. Cuperus, BSc.

Supervision
dr. I. Swart
prof. dr. D. A. M. Vanmaekelbergh

Condensed Matter & Interfaces
Debye Institute for Nanomaterials Science

Master´s thesis - January 2020

Abstract

The quantum mechanical properties of molecules and lattices can be simulated with the scanning tunnelling microscopy (STM), a flat surface and some atoms or molecules on top of it. Manipulation of these atoms by the STM tip allows for the construction of 2D artificial lattices that exhibit properties analogues to their real counterparts. The most established version of these simulators uses the Cu(111) surface and CO molecules adsorbed on top of it. However, the intrinsically strong coupling between surface and bulk states in this system limits the achievable energy resolution. We have investigated the possibility of using supported Bi(111) nanofilms as a novel surface for quantum simulations of this kind.

Surfaces of both Si substrate and Bi nanofilm have been cleaned to yield atomically flat terraces. The electronic properties of grown Bi(111) films have been investigated through STS experiments and DFT simulations. Scatterers were introduced and investigated for their use in constructing artificial lattices. CO molecules are shown to be unsuitable for this function, as they do not adsorb onto the Bi(111) surface. In contrast, Pb and Bi atoms showed signs of being able to fulfil this role: manipulation by the STM tip was performed and scattering of the surface state was observed. The manipulation was, however, not reliable and as such, no artificial lattice is build. Overall, the results presented here are the first in the development of the use of Bi(111) in quantum simulations.

The author can be contacted via LinkedIn or e-mail: j.p.cuperus@students.uu.nl.

Contents

1 Introduction

Advances in science and technique allow for control over increasingly smaller particles. Recent examples are the 2016 Nobel prize in chemistry (molecular motors [1]) and the 2018 Nobel prize in physics (optical tweezers [2]). Whereas these two techniques use light to gain control, other methods are available that allow for control at a similar (or smaller) scale. One of these techniques uses the capability of the scanning tunnelling microscope (STM) to image surfaces and position atoms, both with atomic precision. Already in 1990, Eigler and Schweizer used the STM to arrange Xe atoms on a Ni(110) surface into the IBM logo [3].

The IBM logo might not be particularly interesting, but a whole variety of symmetries and structures can be constructed. When the arranged atoms interact with the surface state electrons, scattering occurs [4, 5]. By combining this scattering effect with the ability to move individual atoms, artificial atoms can be constructed. Confinement of the so-called surface state electrons into a circular arrangement of Fe atoms on a Cu(111) surface resulted in particle-in-a-box behaviour of the electrons [6]. Whereas in real, 3D atoms the electrons are confined by the electric potential generated by the positive nucleus, the electrons in these 2D atoms are confined by the surrounding adatoms. Coupling of the artificial atoms allows for construction of artificial molecules or lattices, through which the properties of corresponding real materials can be simulated. Since the artificial lattice is build up piece by piece, there is a large degree of tunability, through which the properties of the system can be varied. Additionally, the STM allows the electronic structure of the system to be resolved both spatially and spectroscopically. In this way, the quantum state of matter of both well-known and novel systems can be investigated.

For these simulations, the most widely used combination of surface and scatterer is that of Cu(111) and CO. Some examples of lattices/geometries that have been investigated using this system are a molecular graphene [7], a Lieb lattice [8], a quasiperiodic Penrose tiling [9] and a Sierpińksi triangle fractal [10]. However, the energy resolution is intrinsically low, due to the short lifetime of Cu(111) surface state electrons. The presence of CO molecules decreases the lifetime even more. Observation of features thus requires large energy separations. For investigation of phenomena typically associated with small energy spacings, such as spin-split states or self-similarities in fractals, this requirement will impose severe limitations on the experimental feasibility of the simulations.

In the research presented here, we investigated the possibility of using ultrathin Bi(111) films as a new quantum simulation substrate. These films have shown to transport electrons with energy close to E_F exclusively via the surfaces, since the bulk is insulating [11]. Furthermore, the lifted spin degeneracy of the surface state of Bi(111) might allow for investigation of systems that are topologically nontrivial and/or exhibit the quantum spin hall effect. The required steps in the development of the proposed quantum simulator system (substrate preparation, film growth and atom manipulation) have been performed using the STM. Electronic properties of the Bi(111) films have been investigated both experimentally and through DFT calculations.

The outline of this thesis is as follows: first, there is an explanation of the working principles of the STM, a more elaborate introduction of artificial lattices and the material Bi in Chapter 2. Then, the experimental details concerning both STM experiments and DFT calculations will be covered in Chapter 3. In Chapter 4, obtained results will be presented and discussed, before the conclusions and ideas for future research will be presented in Chapter 5 and Chapter 6, respectively.

2 Theory

2.1 Scanning tunnelling Microscopy

The STM is an incredibly complicated and evenly fascinating piece of technology and a complete explanation of its working principles would be outside of the scope of this report. Therefore, only the basics of this technique will be covered at such level that basic knowledge in physics and/or chemistry suffices to understand the research discussed here. For a more elaborate introduction to the technique of the STM, the reader is referred to standard literature, such as *Scanning Probe Microscopy* by Bert Voigtländer, Springer-Verlag [12] or *Introduction to Scanning Tunneling Microscopy* by C. Julian Chen, Oxford University Press [13].

In contrast with other microscopy techniques, such as optical or electron microscopy, scanning tunnelling microscopy does not create direct images of a measured object. Instead, the object is measured in a grid-like fashion by a sharp needle, referred to as the "tip". The tip is brought very close ($< 1\,\text{nm}$) to a surface and scans over it, generating images pixel by pixel. At such small distances, a tunnelling current will flow between the tip and the conducting surface when a bias voltage is applied between the two. Tunnelling is the event where a particle penetrates a spatial region where the potential energy is higher than the particle's energy. This is forbidden by classical mechanics and is thus a purely quantum mechanical phenomenon.

The magnitude of the tunnelling current depends exponentially on the tip-sample distance. As a result, a tenfold increase in tunnelling current can be achieved by decreasing the tip-sample distance by about 1 Å [12]. Together with piezoelectric actuators, through which the tip position above the surface is controlled with pm-precision, this allows for obtaining images with atomic resolution. A simplified electrical circuit of the STM working principle in shown in Fig. 2.1a. From this image, it is clear that the circuit is only closed if the sample is conductive. Insulating substrates can therefore, not be used.

Most commonly, images are obtained by using the STM in feedback mode. In this mode, which is also known as constant-current mode, a feedback loop adjusts the tip height such that the tunnelling current will remain constant. The topography of the tip then represents the topography of the surface, since the tunnelling current depends (to a first approximation) solely of the tip-sample distance.

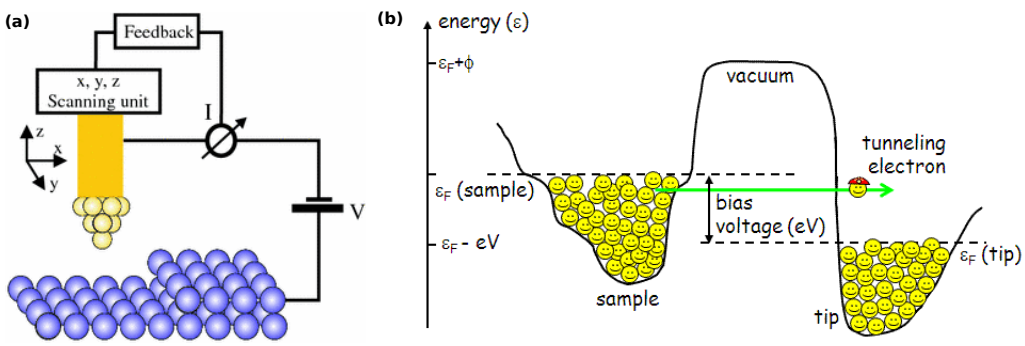

Figure 2.1: (a) Schematic overview of the working principle of the STM, showing the yellow tip that scans over the blue surface. (b) Illustration of the principle of tunnelling in the STM setup, where the electrons are depicted as yellow smileys. Images adapted from [12] and [14], respectively.

Also the electronic properties of the surface influence the tunnelling current. This follows from the fact that an electron can only tunnel from surface to tip, when its energy is between the Fermi level (E_F) and the potential barrier created by the bias voltage. This is schematically shown in Fig. 2.1b. Via the bias voltage, one thus has control over the electrons that will contribute to the tunnelling current and those that will not. As such, at fixed tip height, changes in the tunnelling current are directly proportional to the density-of-states (DOS) of the surface. This allows for direct measurement of the DOS via a technique known as scanning tunnelling spectroscopy (STS).

In STS experiments, the tip height is fixed and the bias voltage V is modulated around a certain set value. Measurement of changes in the tunnelling current I then correspond to the slope of the I(V) curve at the set bias voltage. Since the slope is measured, these experiments are known as dI/dV-measurements. Because of the high lateral resolution achieved by the STM tip, the DOS measured in this way is spatially resolved and therefore referred to as the local DOS (LDOS). By sweeping the voltage while maintaining the (x, y)-position of the tip, one obtains the LDOS as function of energy (a dI/dV-spectrum). Complementary, one can map the LDOS as a function of position, which allows one to show the spatial distribution of electrons at a certain energy (dI/dV-maps).

Atom manipulation

The STM tip is not limited to the characterization of a surface. It can also be used to modify surfaces at will. This was first shown by Eigler and Schweizer, who constructed the IBM logo by patterning Xe atoms on Ni(110) [3]. Today, the manipulation of multiple different species has been reported. Pb atoms and CO molecules manipulated on different surfaces of Cu are examples of this [7, 15]. Even larger structures, such as graphene nanoribbons, have been controllably displaced [16].

For the process of manipulation, two distinctly different modes exist: a lateral and a vertical mode. The lateral manipulation procedure starts by bringing the tip towards the adsorbate that is to be moved, followed by lateral movement of tip and adsorbate. Lastly, the tip is retracted, leaving the adsorbate at its new position. This is schematically shown in Fig. 2.2a. During this whole process, the atom/molecule remains in contact with the surface, which is what distinguishes it from vertical manipulation. In that case, which is shown in Fig. 2.2b, the adsorbate is transferred from the sample to the tip, before being deposited back onto the surface at the desired location.

As might be expected for a event at sub-nm scale, atom manipulation is a very subtle process which requires the right combination of parameters to be successful. By varying the tip-sample distance, bias voltage, tunnelling current and feedback sensitivity, the right balance between the different forces acting on the atom should be found.

If the tip-atom interaction is not strong enough, the atom will not leave its equilibrium position. The tip will then hover over the atom, without altering its position. However, an attractive tip-atom interaction that is too strong will lead to a transfer of the atom to the tip. Although this is

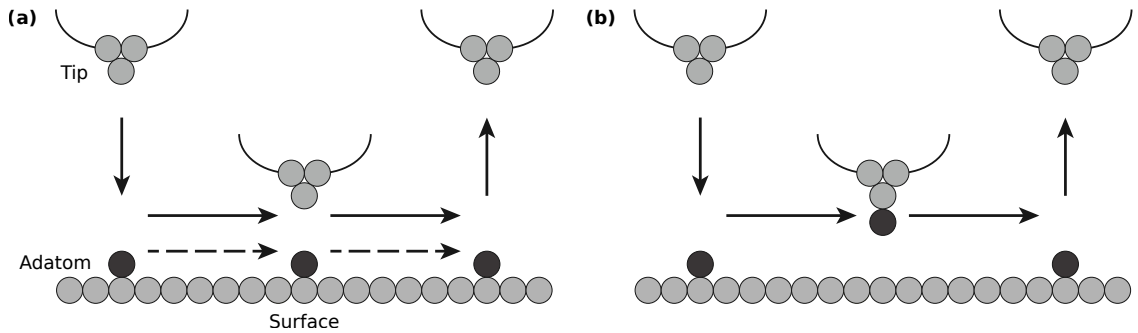

Figure 2.2: Schematic drawings of atom manipulation by the STM tip. In a horizontal manipulation event (a), the atom-surface bond is never completely broken, in contrast to a vertical manipulation event (b).

desired in the vertical manipulation mode, the opposite is true for the lateral mode. For a certain combination of tip and adsorbate, the strength of the forces the two is mostly determined by the distance between them. Therefore, establishing the correct tip height is of major importance. Tip-adsorbate interactions are also affected by the feedback loop sensitivity, since this determines how quickly the tip height is adjusted in response to measured changes in the tunnelling current. By setting the bias voltage and setpoint current, the direction and magnitude of the tunnelling current at a certain tip height can be specified. This allows for control over the excitation of molecular vibrations by the tunnelling electrons [17, 18]. These excitations can alter the behaviour of the adatoms severely.

Verification of what happens during the manipulation process can be obtained in two ways: a first is to scan before and after manipulation. Thereby, one can find out whether the configuration of the atoms on the surface has changed. A second manner, is to investigate the tunnelling current and tip height during the process. Although the feedback loop is enabled during lateral manipulation, a tunnelling current that does not change throughout the whole process is almost never observed. The extremely small time scale on which events on the nanoscale occur is much shorter than the update rate of the feedback loop. Such events will show up in the tunnelling current traces, which can thus contain valuable information.

2.2 Artificial electronic lattices

At the low-index surfaces of noble metals, such as Cu(111) or Au(111), electronic states exists which are localised close to the surface. Just as the valence electrons of these materials, the electrons at the surface can be accurately described as nearly free electrons [19]. Since these electrons solely exist close to the surface, they exhibit two-dimensional behaviour. Consequently, the collective of these electrons is described as a two-dimensional free electron gas (2DEG).

As described by quantum mechanics, electrons posses wavelike character. This also holds for the electrons in these 2DEGs, as was shown by STM experiments: surface state electrons scatter off potential barriers on the surface, such as step edges [20] or point defects [5], resulting in standing wave patterns. Pioneering work was done by Crommie et al., who showed that the electrons of the 2DEG, when confined, exhibited behaviour analogous to the particle in a box model [6]. The (circular) "box" was constructed by Fe adatoms on the Cu(111) surface, which were arranged into a closed ring (see Fig. 2.3a).

This idea was extended by Gomes et al., who confined the 2DEG of Cu(111) in a potential landscape with the same symmetries as graphene [7]. The resulting “artificial graphene” structure is shown in Fig. 2.3b. Experimentally, this was realized by lateral manipulation of CO molecules. The presence of the Dirac cone, characteristic for the electronic properties of graphene, was confirmed by STS experiments (Fig. 2.3c). By imposing the graphene-symmetry onto the 2DEG, the electronic

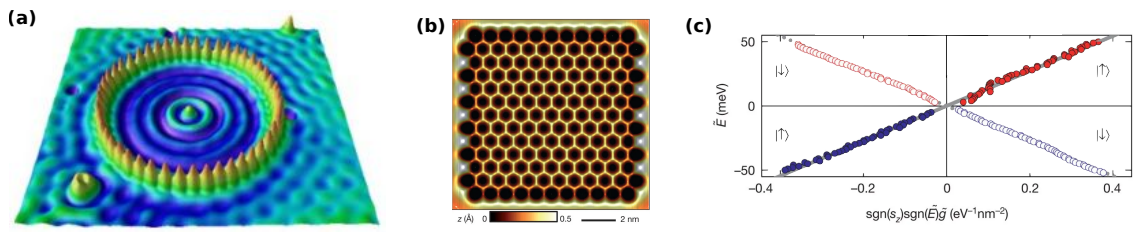

Figure 2.3: (a) Closed ring of Fe adatoms on Cu(111). Standing wave pattern as result of interaction between surface state electrons and scatterers is visible. (b) Artificial graphene structure created by positioning of CO molecules. Black areas consist of multiple CO molecules. (c) Dirac cone as measured in the artificial graphene structure. Images (adapted) from ref. [6] (a) and [7] (b, c).

properties of the solid are inherited with it. Based on this, other lattices and structures have been successfully simulated in the same way. Examples are the Lieb lattice [8] and the Sierpiński triangle [10].

As was directly observed by Gomes et al. in 2012, the energy resolution of the CO/Cu(111) system is relatively low. Thermal broadening effects can be excluded, since the working temperature during these experiments is 4.5 K. Instead, the broadening of the peaks in measured dI/dV-spectra results from the energy-lifetime uncertainty principle. Inherently, electrons of the Cu(111) surface state couple to bulk states. Therefore, they have a lifetime of only 27 fs, which directly translates to a broadening of ca. 23 meV [21]. The CO molecules on the surface facilitate the coupling of surface state electrons to bulk states, subsequently decreasing their lifetime and increasing broadening [22]. This results in a typical experimental broadening of 40-80 meV, depending on the configuration and concentration of CO molecules [7, 10]. This imposes limitations on the features that can be observed in dI/dV-spectroscopy. It has been proposed that new substrates should be investigated to overcome this problem [23].

2.3 Bismuth

Decreasing surface-to-bulk coupling is expected to result in an improved energy resolution. A way to decrease this coupling is to decrease the amount of bulk states close to the Fermi level. To this end, we propose the use of thin Bi(111) films as a new substrate. Because of their semimetallic nature, Bi films meet both agreements for STS experiments with high resolution. The small overlap between valence and conduction band allows for electron transport at arbitrary voltage, while simultaneously decreasing surface-to-bulk coupling. In addition, the reduced amount of bulk material in thin films also decreases the number of bulk states. Moreover, the (111)-surface of bismuth hosts a surface state, which in principle would thus allow for the construction of artificial electronic lattices [24–26].

The crystal structure of bismuth is typical for the group V semimetals and has rhombohedral symmetry. Strong and weak interatomic bonds are alternated in the [111]-direction, resulting in a bilayered structure, which is shown in Fig. 2.4a. Subsequently, the Bi(111) surface is always terminated by a bilayer and never by a single layer of Bi atoms [28]. A top view image of the (111) surface is shown in Fig. 2.4b, showing the 2D unit cell of the uppermost layer of atoms. Only these atoms are visualized in STM topographs with atomic resolution [29].

The electronic properties of Bi, being a heavy element, are heavily influenced by spin-orbit coupling (SOC). In the absence of inversion symmetry, this relativistic effect lifts the spin degeneracy in the electronic structure of materials [27]. The rhombohedral structure of bulk Bi does have inversion symmetry, which means that its bands structure remains spin degenerate. However, this inversion

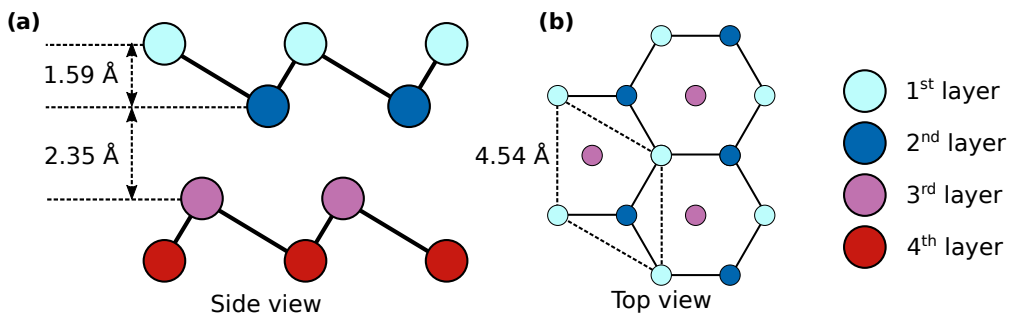

Figure 2.4: Structure of bulk Bi. (a) Side view of the structure shows the bilayers and the alternating short and long distances. (b) Top view shows the (111) surface and its threefold symmetry. 2D unit cell is drawn by dashed line. Lattice constants are shown in both. Adapted from ref. [27].

symmetry is lost at the surface, leading to splitting of the surface states via the Rashba effect [30, 31]. Qualitatively, this effect can be understood by realizing that the abrupt termination of the bulk structure results in a potential gradient perpendicular to the surface. In analogy to the case of SOC, this will result in a splitting of states by coupling to the spin of the electrons. The influence of the Rashba effect on the band structure of a 2D free electron gas is shown in Fig. 2.5.

The spin-resolved surface state of Bi(111) might allow for simulations where the spin is of importance. Examples are spin-spin interactions or the quantum spin Hall effect. Because the energy differences associated with spin-induced effects is typically small, the proposed high energy resolution of Bi(111) will be needed to ensure experimental success.

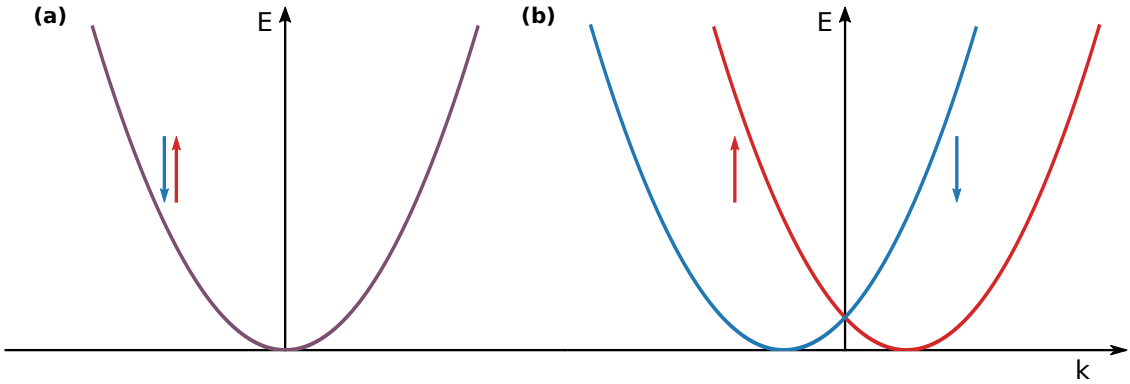

Figure 2.5: Band structure of a free electron gas in the absence (a) or presence (b) of the Rashba effect. The parabolic energy dispersion remains intact, but the spin degeneracy is lifted by a horizontal shift of the curve.

3 Methods

3.1 STM experiments

All experiments presented in this thesis have been performed on a Sigma Surface Science POLAR SPM, which is shown in Fig. 3.1. Sample preparation and measurements were performed under ultra-high vacuum (UHV) conditions. Base pressures in the preparation and SPM chamber were below 1×10^{-10} mbar and 5×10^{-10} mbar, respectively. PtIr and W tips, covered with surface material were used in all measurements, which were conducted at 4.5 K. Acquired images are processed used the gwyddion software [32].

Si(111) surfaces were prepared using polished, <111>-oriented and B-doped Si wafers and standard flash-annealing cycles. Newly inserted samples were degassed for 1 h at 600 °C using a Teflon resistive heating plate situated underneath the sample plate. The sample was then heated for 6 h at 900 °C which was reached through direct-current (DC) heating. To obtain a flat Si(111)-7x7 reconstructed surface, flashing cycles were applied. For performing these cycles, the sample was first heated to 900 °C. When this temperature was reached, the wafer was heated to 1200 °C by increasing the DC current abruptly. This resulted in a increase in pressure and the temperature was maintained until the pressure exceeded 1×10^{-9} mbar. This procedure was repeated until flashing times of ca. 30 s could be achieved.

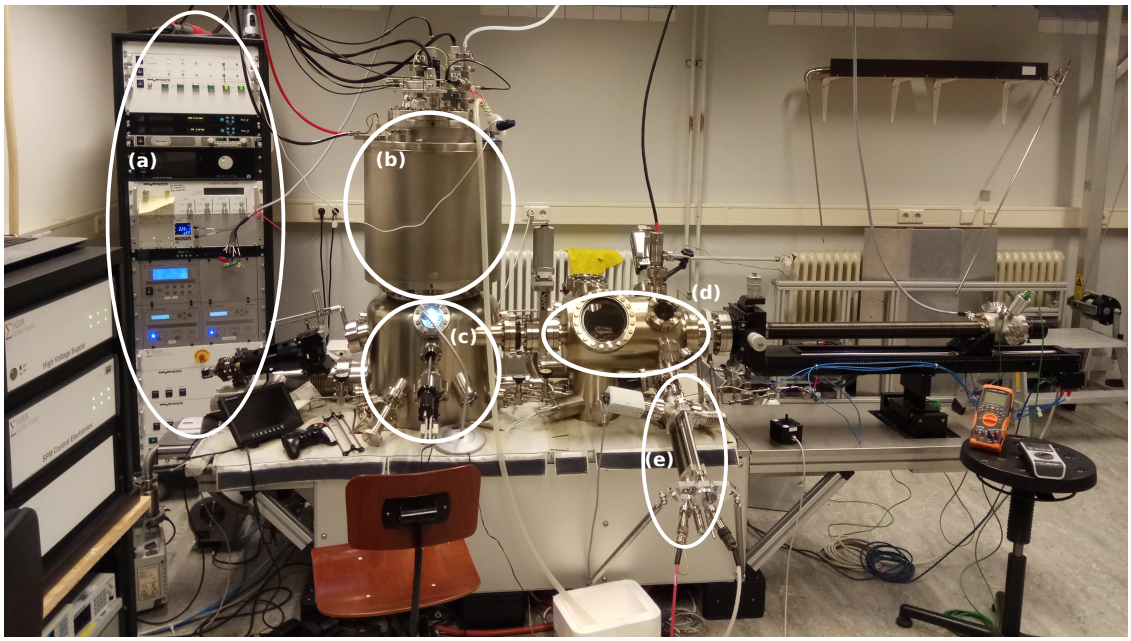

Figure 3.1: STM setup used for all STM experiments presented in this thesis. Some components of the microscope have been highlighted: (a) Electronics rack, used to control the machine. (b) Bath cryostat that keeps the measuring head at 4.5 K. (c) STM chamber, part of microscope where data is acquired. (d) Preparation chamber, part of microscope used for preparation of samples. (e) Evaporator used for the growth of Bi films. Adatoms are deposited from a similar device, situated at the back of the STM chamber (not visible).

For the growth of Bi(111) films, a MANTIS Deposition QUAD-EV-C Mini e-beam evaporator (Fig. 3.1e) was used, which was mounted onto the preparation chamber. Elemental bismuth was used as the source and the estimated evaporation rate was 0.2-0.4 ML/ min. Post-evaporation annealing (130 °C, 6 h) via the resistive heating plate was used to increase the flatness of the Bi films.

Atom deposition was performed using a MANTIS Deposition M-EV Mini e-beam evaporator, mounted onto the SPM chamber. This allows for evaporation onto a sample which is cooled to 4.5 K. Exact evaporation parameters were changed between different experiments, but sub-ML amount of material were deposited in all cases. Some parameters, specific to our STM setup, used in the processes described above, are listed in Appendix A.

dI/dV-spectroscopy experiments were performed using a lock-in amplifier operating at 973 Hz. Spectra were composed of 401, 601 or 801 data points and a modulation amplitude of 100 mV was used. The acquisition time per data point was either 100 ms or 250 ms.

3.2 DFT calculations

Ab initio theoretical simulation were performed using the SIESTA code (trunk-786 version) [33] in combination with the generalized gradient approximation (GGA) function of Perdew, Burke and Ernzerhof (PBE) to describe to exchange-correlation potential [34]. SOC coupling was implemented in all calculations via the off-site approximation as described in ref. [35]. The 6s and 6p electrons of Bi were taken as the valence electrons and are described by a DZP basis set. A soft confinement potential was used for the 6p orbital [36]. Additionally, the 5d electrons were included as semicore electrons described by a single ζ-function. All other electrons are described by a fully relativistic, norm-conserving pseudopotential [37]. A mesh-cutoff of 400 Ry was used for all calculations and the Brillouin zone was sampled by a 11 x 11 x 1 Monkhorst-Pack k-point grid [38] (11 x 11 x 11 in the case of bulk Bi).

Optimization of the basis set was performed on the bulk Bi system. Structural parameters from ref. [27] were used, without structural relaxation. Basis set parameters were varied to match the experimental work function of 4.22-4.25 eV [39] and the electron (27.2 meV) and hole pockets (10.8 meV) at high symmetry points L and T, respectively [40]. Our simulations calculated a work function of 4.22 eV and an electron (hole) pocket depth of 24 meV (14 meV). The resulting band structure is shown in Fig. 3.2.

To perform simulations on Bi films, slabs of 10 BL were used. Vacuum was inserted to decouple the slabs (the calculation is periodic in all 3 dimensions) and a slab-dipole correction was applied to cancel the artificial electric field induced by this [41]. The system was relaxed in the direction of the surface normal, until the atomic forces were smaller than 0.1 meV $Å^{-1}$. The structural relaxation was performed using a conjugate-gradient optimization method in which the position of the lowest atom in the slab was fixed. In some cases, the film was terminated by hydrogen atoms (DZ2P basis set) placed at a fixed distance of 2 Å beneath the lowest Bi atom in the slab. Hydrogen atoms were only added after relaxation of the freestanding slab. An example of a SIESTA input file can be found in Appendix B. Processing of the DFT output was performed using SIESTA tools and the sisl package [42].

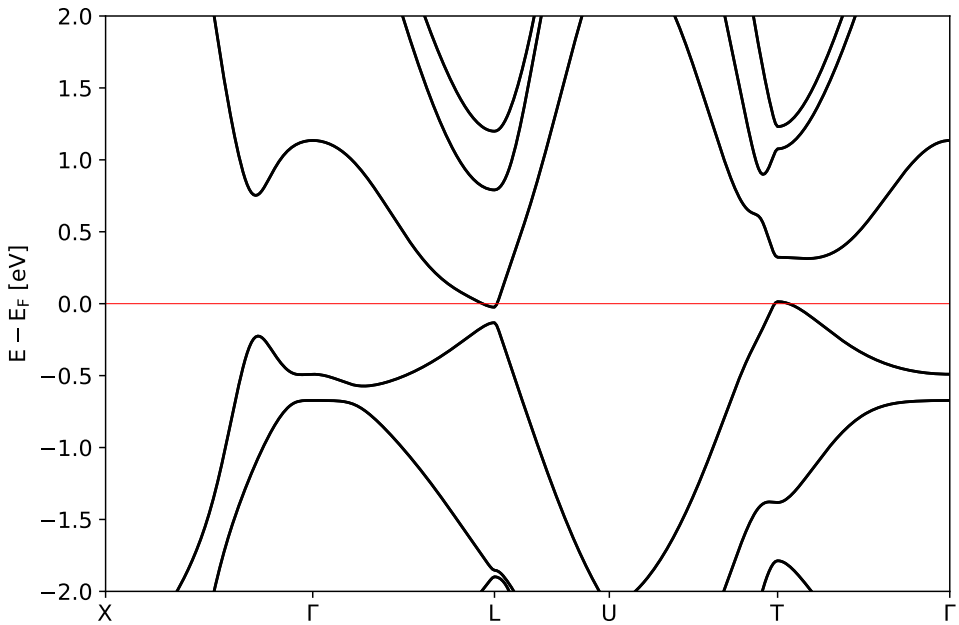

Figure 3.2: Band structure of bulk Bi as calculated via the method explained above. Red horizontal line represents the Fermi level.

4 Results and Discussion

The obtained results can be assigned to different stages of the assembly of the quantum simulator system. First, the preparation of the Si wafer will be covered, followed by the experiments concerning the growth of the Bi films. Subsequently, the investigation of the electronic properties of grown films, is discussed. Lastly, three different potential scatterers are introduced.

4.1 Si(111) surface

Although obtaining a flat Si(111) surface through the flash/anneal procedure is a very well-known process [31, 43–46], this was never performed in our setup before. Central in this procedure are the flashing cycles, during which the wafer is rapidly heated to 1200 °C for short periods of time.

Using this procedure, we were able to create flat Si(111) terraces with sizes exceeding 600 nm x 600 nm, as can be seen in Fig. 4.1a. The 7x7 reconstruction is clearly visible, next to some adsorbates, defects and grain boundaries.

We assume that a surface as shown in Fig. 4.1 is of sufficient quality to be used as a substrate for Bi nanofilms.

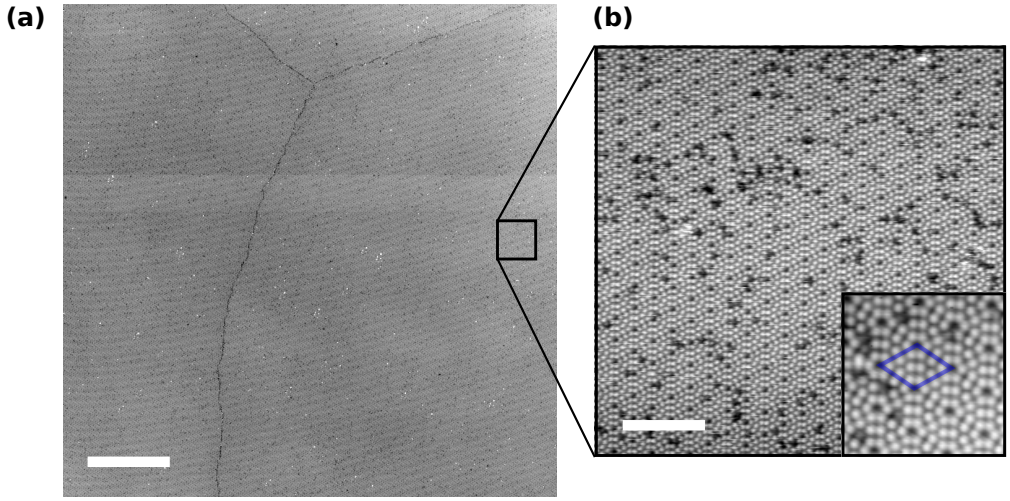

Figure 4.1: STM topographs of the prepared Si(111)-7x7 surface. (a) Shows the flatness of the surface on a large scale and the presence of grain boundaries. (b) A zoom in shows the 7x7 reconstruction together with some missing atoms and adsorbates. Inset of (b) shows the unit cell of the reconstructed surface (blue). Scale bars represent 100 (a) and 10 nm (b). Acquisition settings are 1 nA and 3.0 V (a), 2.0 V (b) and −0.7 V (inset).

4.2 Bi(111) growth

With the flat Si(111) surface at hand, we could turn to the fabrication of ultrathin Bi films. Problematic was the absence of a method that (directly) allows for determination of the amount of deposited material. Most commonly, a quartz microbalance is used for this purpose [11, 43, 45, 47], but also Rutherford backscattering has been used [31, 48–50]. However, the only quantification method available in the used setup, is a flux meter in the evaporator. Since this meter needs to be calibrated, the initial evaporation attempts have been a shot in the dark.

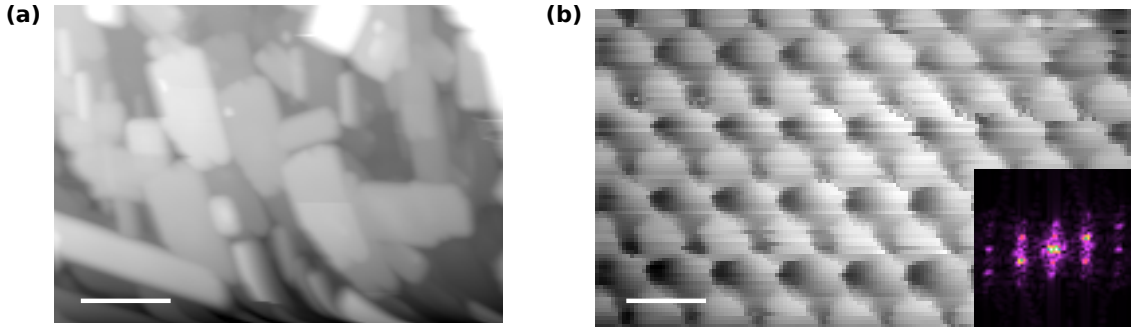

Figure 4.2: (a) STM topograph of Bi film with initially unknown thickness. The observable, patched structure is also observed in ref. [29] for a Bi film of 2-4 ML. (b) STM topograph of the same film with atomic resolution, revealing the pseudocubic phase observed in the 4 ML thick samples of ref. [48]. Scale bars are 10 nm and 0.5 nm for (a) and (b), respectively. Both images are acquired at 1 nA and 2.0 V.

When one of these initial films was investigated, its surface showed a patched morphology, as can be seen in Fig. 4.2a. This surface structure shows similarity to the surface of a 2 monolayer (ML) thick bismuth film as measured by Nagao et al. [29]. In a another paper of the same group, atomic resolution images of a 4 ML thick Bi film are presented, showing a pseudocubic arrangement [48]. This arrangement was also observed for our Bi film, as can be seen in Fig. 4.2b. Hence, we concluded that the used evaporation procedure resulted into a Bi film with a thickness of 2-4 ML, which was used to calibrate the flux meter.

New Bi films were grown with an estimated thickness of 15-30 ML using an evaporation rate of 0.2-0.4 ML/ min. After evaporation, the sample was annealed using the resistive heating plate for 6-8 h at 130 °C, as measured by the thermocouple situated on the manipulator arm. In Fig. 4.3a, an overview scan of the resulting surface is shown, revealing the tendency of Bi to form triangular islands [45]. Since the triangles in this figures show only two different orientation, it seems as if the formed Bi film is single-crystalline. This is in line what has been reported [50]. The investigated area is however, relatively small and other techniques measuring larger areas, for example electron diffraction, should be used to determine the crystallinity of the film.

Atomically flat terraces with sizes larger than 50 nmx50 nm have been found. Although Bi(111) surfaces with larger terraces have been reported [25], showing that the evaporation/annealing procedure can be further optimized, the observed terrace sizes are satisfactory for our purposes. On small scales, atomic resolution was accomplished, showing the hexagonal structure adopted by the topmost layer of Bi atoms (Fig. 4.3c).

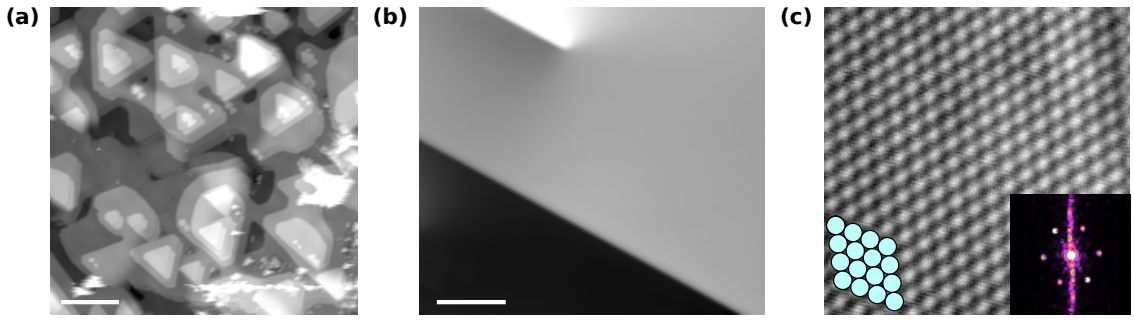

Figure 4.3: STM topographs of a Bi(111) film with nominal thickness of 15-30 ML. (a) The tendency of Bi(111) to form triangular islands is visible. From the orientation of the island, we deduct that the Bi film is single crystalline (at least at this scale). Scale bar represents 50 nm. (b) The flatness of a terrace can be observed, showing that the surface is atomically flat. Scale bar is 10 nm. (c) A clean area of Bi(111) on which atomic resolution was obtained. The hexagonal pattern arising from the topmost layer of Bi atoms is visible both in real space and in the Fourier transform (inset). Blue circles are a schematic representation of the Bi atoms.

4.3 Electronic properties of Bi(111)

To investigate the electronic properties of the grown films, we conducted dI/dV-measurements. DFT simulations were performed to reproduce the experimental data ab initio, additionally allowing for investigation of the measured properties in ways not accessible through STS.

Surface state

At first, we have probed the electronic structure of the Bi(111) films by STS experiments on clean/flat areas, where we expect to observe signatures of the surface state. In the resulting spectra, one of which is shown in Fig. 4.4a, the surface state contributions are clearly visible [25, 51]. By calculating the DOS of the topmost layer of a H-terminated 10 BL thick slab, we have attempted to simulate the measured LDOS. The result of this, also shown in Fig. 4.4a, reveals that there is a good match between the experimental and theoretical data. Measured peaks are reproduced, together with some additional states. The energy difference between the peaks at ca. +200 meV is only 20 meV and the difference between those at E_F is even less. Plotting the charge density of a surface state wave function, as is presented in Fig. 4.6a, shows the localisation at the upper surface of the film.

The two biggest discrepancies between the theoretical and experimental data, are the peaks at −0.25 eV and +0.15 eV. The corresponding band structure of the system (Fig. 4.4b) can be investigated to gain more information on the origin of these peaks. This shows that both peaks correspond to electronic states close to the $\overline{M}$-point. A possible explanation for the observed differences might be the low sensitivity of the STM for electronic states away from $\overline{\Gamma}$ [12]. Additionally, the electronic structure of Bi thin films at $\overline{M}$ has been unclear for quite some time already [27]. DFT simulations on thin films have proven not to be decisive, since it is arguable whether or not the film should be terminated with H-atoms [31].

The function of the termination layer is to simulate the effect of the underlying substrate on the electronic properties of the ultrathin film. However, the electronic coupling between the wafer and the film is relatively weak, due to the presence of a wetting layer [49]. As such, termination might be unnecessary and indeed, many reports include theoretical simulations on freestanding slabs [25, 47, 52, 53]. Also these simulations, for example in the case of ref. [25], are able to match measured dI/dV-curves very accurately. In our case however, the match between the theoretical and experimental data seems to justify the choice to terminate the slab with hydrogen atoms. This is confirmed by simulations in the absence of hydrogen atoms (see below). Although the addition of the H-atoms to the bottom might seem to be a small change, its effect on the surface state is large: the termination removes the inversion symmetry from the system, which is required for Rashba-effect induced spin-splitting of states.

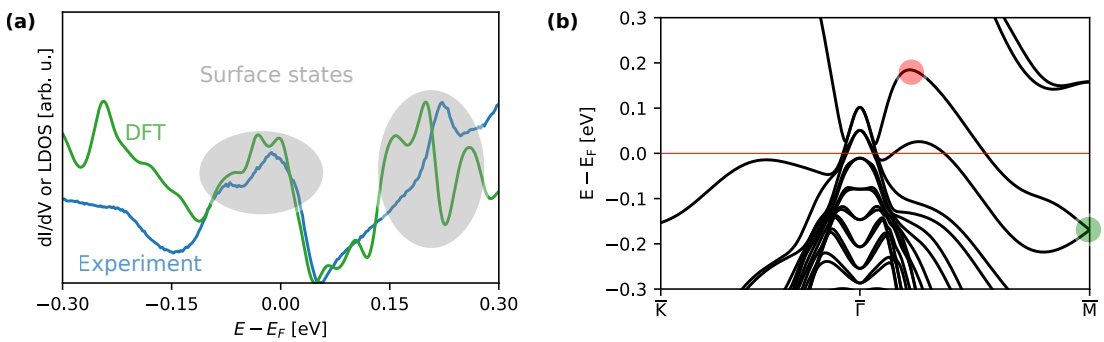

Figure 4.4: (a) Experimental dI/dV-curve acquired on a atomically flat area of Bi(111) (blue) and LDOS at topmost layer of Bi atoms, as calculated by DFT (green). Peaks with high surface state contributions are visible from −100 to +50 meV and at +200 meV. (b) Calculated band structure for a 10 BL thick Bi(111) slab. Red and green dots correspond to wave functions used for charge density plots in Fig. 4.6.

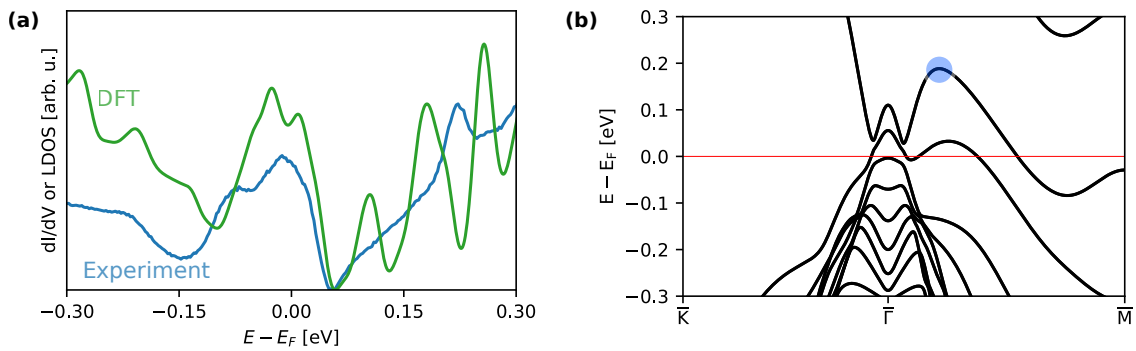

Figure 4.5: (a) Experimental dI/dV-curve (blue) and calculated DOS of the toplayer of atoms in a freestanding slab of 10 BL (green). Blue curve is identical to that in Fig. 4.4a. The match between the simulation and experimental is worse than in Fig. 4.4. (b) Band structure of the slab described above. Blue circle represents wave functions that are used for charge density plot of Fig. 4.6.

For comparison, we calculated the electronic properties of a 10 BL Bi slab without H-termination, the results of which are shown in Fig. 4.5. From the LDOS, it is immediately clear that this situation is a worse description of our experimental data. The band structure is completely spin degenerate, but degenerate surface states are physically separated, as can be seen in Fig. 4.6c, d.

Our results are in line with those of ref. [31], where ab initio calculations with and without H-termination are compared with band structures measured by angle-resolved photoemission spectroscopy (ARPES). They have shown that the SO-split character of the bands from $\overline{\Gamma}$ in the direction of $\overline{\mathrm{M}}$ can be reproduced by simulations of H-terminated slabs. However, to match the experimental band structure close to the $\overline{\mathrm{M}}$-point, it was better to simulate the Bi films as if they were freestanding. Terminated slabs produced a worse description of the experimental data, but at **k**-vectors closer to $\overline{\Gamma}$, the match was not as good as obtained before. We have obtained similar results: except for the features originating from **k**-points close to $\overline{\mathrm{M}}$, the theoretical simulations of H-terminated films can reproduce the experimental data very well.

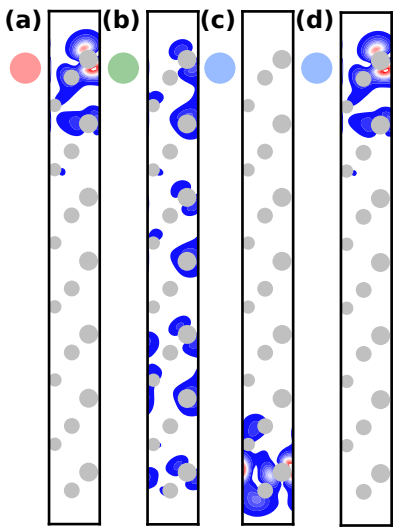

Figure 4.6: Charge density plot showing that specific electronic states are either surface states or delocalized over all layers of the film. (a) and (b) are states from the H-terminated slab, using states between $\overline{\Gamma}$ and $\overline{\mathrm{M}}$ (a) and at $\overline{\mathrm{M}}$ (b). (c) and (d) are electronic states with opposite spins with k vector on $\overline{\Gamma\mathrm{M}}$. Corresponding states in the band structures can be found via the color coded circles next to the plot.

All in all, we prefer to simulate the grown films, since these simulations resulted in the best match with the experimental data. The observed differences can be explained via the lower sensitivity in STM experiments towards electrons with in-plane momentum. Our preference is in contrast with literature, where Bi films grown on Si(111) are typically modelled by freestanding Bi slabs. This finding might be explained by the absence of the wetting layer, that decouples the film from the substrate. However, we have not conducted experiments that could prove whether this layer is present or not. It might also be that the electronic coupling between the Bi film and the underlying substrate is dependent on the **k**-vector. The termination with hydrogen atoms is only an approximation of the real situation and will therefore have its limits. More insight into this might be obtained by inclusion of the Si wafer in the modelling of the ultrathin films. Also STM experiments could aid in resolving this issue. Fourier transforming dI/dV-maps in which surface scattering is observed, allows for reconstructing of the surface band structure [54, 55].

Scattering of the surface state

For the construction of artificial electronic lattices, it is essential for the adsorbates to interact with the surface state. As can be seen in Fig. 4.7a-c, we can clearly observe a scattering pattern close to impurities in/on the surface. The Pb atoms in Fig. 4.7a shows a scattering pattern that possesses threefold symmetry, which is also observed close to a small defect (Fig. 4.7b). The anisotropic pattern can be explained when the Fermi surface of Bi(111) slabs is considered, including the spin moments associated with the electronic states in it. The sixfold symmetry of the Fermi surface, which is shown in Fig. 4.7d, and the requirement of spin-moment conservation, restricts the scattering to occur in six directions [56]. It is proposed that the sixfold symmetry is reduced to the observed threefold symmetry by the underlying lattice, which is also threefold symmetric. In Fig. 4.7c, where the scattering center is somewhat larger, the scattering pattern approaches an isotropic shape and a clear standing wave pattern appears. The absence of the threefold symmetric scattering pattern means that this scatterer cannot be classified as a point scatter.

A triangle formed by three Pb atoms was encountered on which dI/dV-spectroscopy was performed, to compare the LDOS inside the triangle with that of a clean Bi(111) surface. The locations where the spectra are acquired and the resulting spectra are shown in Fig. 4.7d and f, respectively. Data of three spectra is averaged and the two curves have been vertically shifted such that they match at $V = -0.5\,V$. In the curve of the clean surface (orange), the peaks with high surface state contributions can be recognized. If the surface state electrons would be confined by the Pb adatoms, it is to be expected that these electrons have increased energies. In that case, we expect to be able to match each of the peaks in the green curve to its non-confined counterpart in the orange curve. Where the position of the peak at ca. $-0.25\,V$ does show almost no shift upon confinement between the Pb triangle, the peaks just before $0\,V$ seem to have shifted to slightly higher energies. Two distinct peaks can now be observed, showing that different electronic states interact differently with the adatoms. We tend to interpret this increase in energy as the result of particle-in-a-box behaviour of surface state electrons in the Pb triangle.

The most logical match of the peak at $0.2\,V$ (clean Bi) would be the peak at slightly lower energy in the spectrum of the confined case. This choice is supported by the similar slope for both peaks. In contrast, the decrease in energy of this state upon confinement is unexpected and cannot be explained by the idea of quantum confinement. However, the observation of a peak just before the onset of the surface state can be explained by the idea of localisation at an adatom. If an atom acts as an attractive potential for the surface state electrons, they can lower their energy by localizing at this atom. This effect is already known to exist for Cu and Cs adatoms on the (111) surface of Cu [57, 58]. Whether localisation of the surface state also occurs in this situation, might be explained by spectroscopy experiments in the vicinity of single adatoms. The few measurements we performed however, turned out to be inconclusive due to experimental flaws.

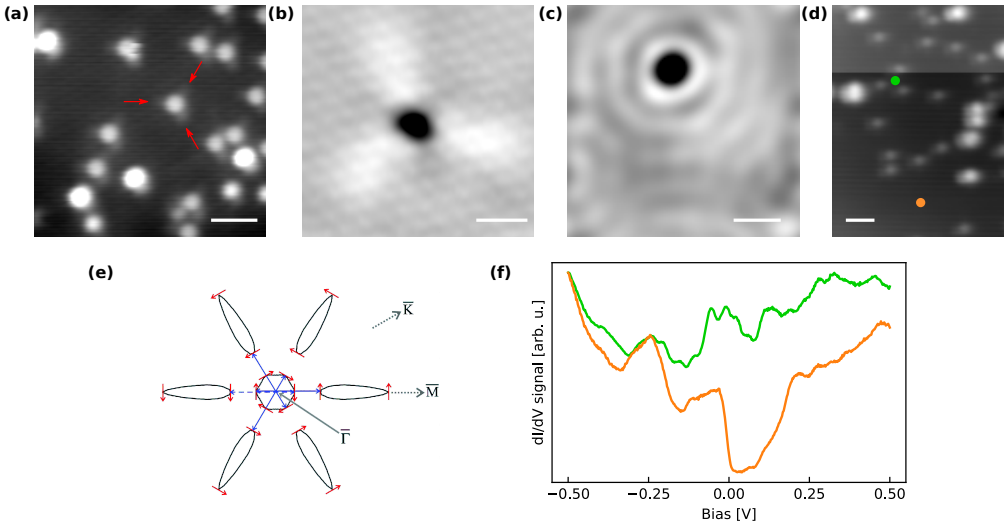

Figure 4.7: (a-c) STM topograph that show the scattering of the surface state on Pb atoms (a) and missing atoms (b, c). Scattering is clearly anisotropic in (a) and (b), whereas it is nearly isotropic in (c). (d) STM topograph showing the triangle formed by three Pb atoms. The sudden change in contrast is an measurement artefact. Scale bars are, from left to right, 2, 2, 3 and 2 nm. (e) Schematic representation of the Fermi surface of Bi(111) where the direction of the spin moment is denoted by the red arrows. Scattering vectors are drawn in blue. Adapted from ref. [56]. (f) Experimental dI/dV-curves of acquired at a clean Bi(111) surface (orange) and inside the Pb triangle (green). Exact locations where measurements are performed are shown in (d) using the same color coding.

Edge state

Bi islands are known to host a (topologically protected) 1D edge state at one edge type, which is absent on the other edge [28, 46, 47]. This edge state can be found at +183 meV, just before the onset of the surface state. When we compare the spectra acquired at the two different edges, with that of a clean Bi(111) surface, we can also see this state appearing on one of the two edge types (see Fig. 4.8a). The other edge type shows an almost featureless dI/dV-curve at positive bias, in accordance with the findings reported in literature.

We attempted to reproduce the experimentally obtained data through DFT calculations. To create the edge geometry, the strategy of ref. [47] was used. A unit cell of 8 x 1 x 8 Bi atoms is created, from which four Bi atoms of the topmost bilayer are removed. The presence of the edge state is confirmed by the charge density plot shown in Fig. 4.8b. Unfortunately, we have not been able to generate the band structure showing the 1D edge state, due to problems concerning the orientation of the edge direction with respect to the unit cell. The band structure could be interesting for further understanding of the nature of the edge state.

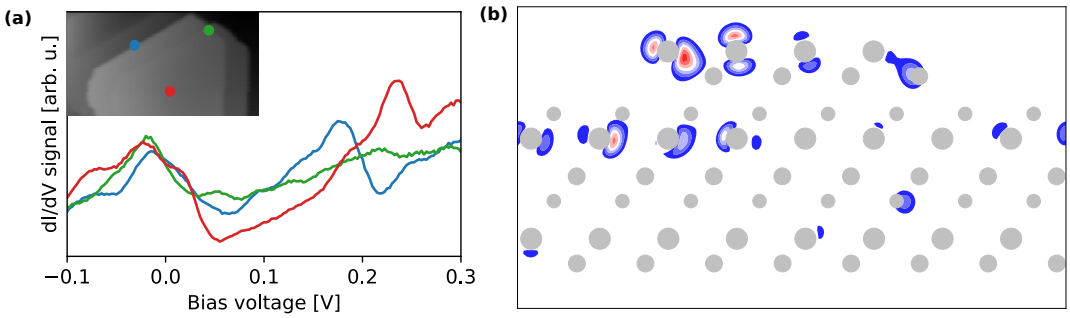

Figure 4.8: (a) STS experiments data acquired on two edge types and clean Bi(111) surface, as indicated by the color coding in the inset. Shown island is ca. 30 nm in width. (b) Charge density calculated for a **k**-vector parallel to the edge, with E = +84 meV.

4.4 Adsorbate introduction: CO

The Cu(111)/CO tandem has shown to be a versatile system for the construction of artificial electron lattices [7, 10]. Therefore, we have attempted to extend the use of CO as a point scatterer to the Bi(111) surface. We have employed a similar evaporation procedure as is common for the Cu(111) surface: CO gas is leaked into the SPM chamber up to a pressure of 1.5×10^{-8} mbar. The sample is already inside the measuring head (at 4.5 K) and protected from the CO gas by closed isolation shields. The shields are then opened such that there is a direct line of sight from the CO source, towards the sample. Assisted by the cryopump effect of sample and measuring head, the CO gas flows towards the surface, where some of it is expected to stay put. By controlling the time for which the shields are opened, one can control the CO coverage.

In Fig. 4.9a, a Bi(111) surface is shown which has been exposed to CO for 5 min. Unexpectedly, no CO molecules were observed on the Bi surface. An identical procedure yields a clear CO coverage on Cu(111) after 3 min of evaporation, as is shown in Fig. 4.9b. This shows that the applied method is suitable for the evaporation of CO and that the absence of it must be due to the properties of the Bi(111) surface. We have acquired images at multiple different voltages, as it is known that the bias voltage can have a large influence on the way adsorbates are imaged [59, 60]. However, the result remained unchanged.

Qualitatively, we can understand this finding by looking at the molecular orbitals (MOs) of the top surface atoms and the CO molecules. On Cu(111), CO binds to a top-site position, where the carbon atom of CO binds to a single Cu atom of the surface. The highest occupied MO (HOMO) of CO, which is mainly localized at the carbon atom, typically establishes the bond between CO and another species by donation of its electron density. In the case of Cu(111), the Cu-CO bond is established by the donating interaction from the CO molecule into the partially filled s-band of Cu [61].

Looking at the valence orbitals of Bi atoms in the top layer of Bi(111), one can see that it has three nearest-neighbours which are found in the layer below it. From the picture of covalent bonding, this atom is similar to the nitrogen atom in ammonia (NH_3). Both the elements bismuth and nitrogen are group XV elements, which means the valence electron configuration is ns^2, np^3, where $n = 2$ for N and $n = 6$ for Bi. From a molecular bonding picture, Bi atoms at the surface may therefore be expected to have a lone pair of electrons (dangling bond) parallel to the surface normal. If a CO molecule were to bind on Bi(111) in the same way as it does on Cu(111), this would result in electron repulsion between the lone pair on the Bi atom and the HOMO of CO.

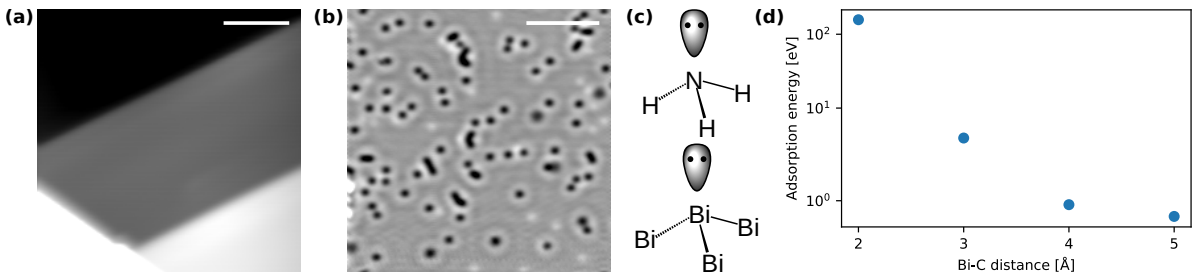

Figure 4.9: (a) STM image of Bi(111) surface exposed to a CO atmosphere, but shows no signs of any adsorbates. Terrace in bottom-left is placed out of color scale to increase contrast in rest of image. (b) STM image of Cu(111) exposed to a similar atmosphere. (c) Simplified geometrical and molecular structure of ammonia (upper) and Bi surface (lower). Both are proposed to have a dangling bond/lone pair that leads to a repulsive interaction with CO. (d) Adsorption energy versus distance to surface for CO on Bi(111), as calculated by DFT. Both scale bars are 5 nm.

Through DFT simulations, the explanation proposed above was confirmed. A CO molecule was placed at several Ås above a relaxed Bi(111) slab and a single point calculation was then performed. Comparison of the total energy of these systems with the total energy of an empty slab and an isolated CO molecule allows for calculation of the adsorption energy. In Fig. 4.9d, the total energy as function of the Bi-C distance is plotted, showing that the adsorption energy is never smaller than zero and quickly increases with decreasing distance. Adsorption of CO on a top-site of Bi(111) is thus energetically unfavourable.

Other adsorption geometries are quickly and qualitatively discussed. Side-on (η_2) coordination, where both the C and O atom of CO bind to the same Bi atom, is forbidden by symmetry of the MOs of CO. Adsorption onto two adjacent Bi atoms would in principle be possible, but the large difference between CO bond length (1.13 Å, [62]) and the Bi-Bi distance in the topmost layer of the slab (4.54 Å, [27]) also makes this unlikely (especially at 4.5 K). Other adsorption positions, such as step edges, are less readily understood and therefore not discussed. Moreover, CO molecules need to be stable at flat parts of the surface to be useful for the construction of artificial lattices.

4.5 Adsorbate introduction: heavy atoms

Not only molecules, but also adatoms have shown to scatter surface state electrons. For example, Crommie et al. constructed a quantum corral by scattering of the Cu(111) surface state on Fe adatoms [6]. Following this strategy, we have evaporated sub-ML quantities of Bi and Pb atoms on Bi(111) and subsequently attempted to manipulate adsorbed atoms using the STM tip.

Using an e-beam evaporator, we deposited either Pb or Bi atoms onto Bi(111) while keeping the sample as cool as possible (< 20 K). The resulting Pb coverage is shown in Fig. 4.10a, where the adsorbates are mainly single atoms. In the case of Bi, the coverage was somewhat higher and a mixture of single Bi atoms and small Bi clusters were found (see Fig. 4.10b).

In principle, both adatoms and adsorbed clusters can be laterally manipulated by the STM tip [63]. However, no reports are known to us where adsorbates are manipulated on Bi(111). We have tried to controllably displace Bi clusters and Pb & Bi atoms using both lateral and vertical manipulation. Obtained results showed very similar behaviour for Bi atoms, Bi clusters and Pb atoms. Therefore, manipulation of all three will be discussed simultaneously. Our strategy is as follows: we choose a certain bias voltage and try to manipulate an adatom using a relatively low setpoint current. If the configuration of the atoms on the surface remains unchanged, we repeated the procedure with a slightly increased setpoint current to decrease the distance between tip and surface. In this way, we controllably increase tip-adatom interaction strength. We repeat this procedure until the configuration on the surface does change, either by lateral manipulation, sample-to-tip transfer or tip-to-sample transfer.

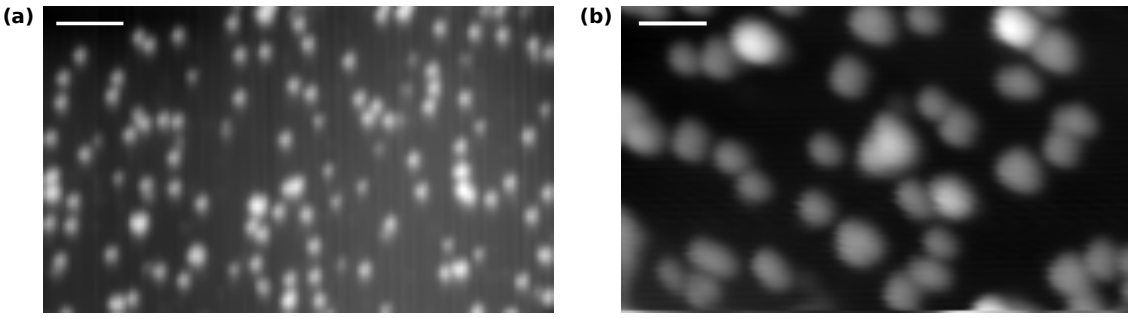

Figure 4.10: STM images of the Bi(111) surface after evaporation of Pb (a) and Bi (b). Single adatoms are mostly found in the case of Pb, based on the similarity and size of the observed adsorbates. A combination of single adatoms and small clusters of Bi can be observed in (b). Scale bars are 4 nm and 2 nm, respectively.

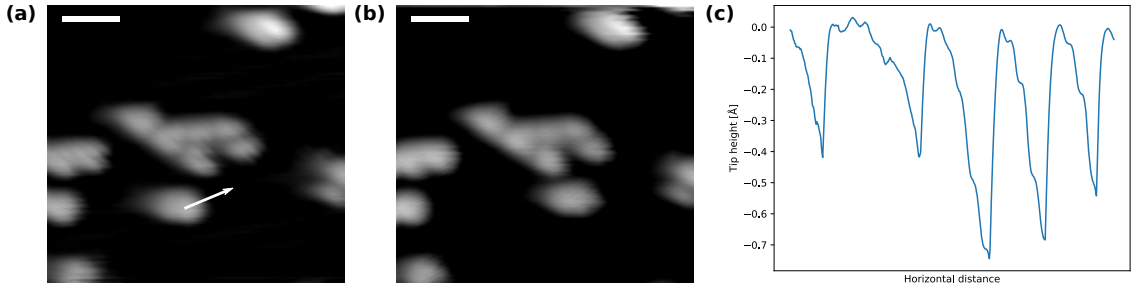

Figure 4.11: STM topographs before (a) and after (b) the lateral manipulation performed on the Bi cluster. (c) Tip height during manipulation, elucidating that the blob was manipulated according to the pulling mechanism.

Lateral manipulation

We have started with attempts at manipulating the adatoms laterally. One of the successful lateral manipulation attempts was performed on a small cluster consisting of several Bi atoms. Its success was confirmed by the topographs acquired before and after the manipulation, which are shown in Fig. 4.11a/b. A bias voltage of −0.3 V and a setpoint of 12 nA were used in this attempt. The tooth saw pattern in the trace (Fig. 4.11c) suggests that the manipulation was performed via the pulling mechanism as described by ref. [63]. In case of the pulling mechanism, where the adatom is pulled over the surface by the tip, the net force between tip and adsorbate is attractive. The trace can then be explained as follows: starting from a position on top of an atom, tip-sample distance is decreased to maintain the tunnelling current setpoint. The closer the tip gets to the surface, the larger the horizontal component of the attractive tip-adsorbate force. At a certain moment, this force is big enough to pull the adsorbate towards the tip onto a new adsorption site. Because this process is extremely fast, there is a sudden increase in tunnelling current because the adsorbate is now much closer to the tip. Based on the irregularity of the tooth saw pattern seen in the trace (Fig. 4.11c), we conclude that the manipulation direction does not follow a high-symmetry direction of the surface.

The same process also occurs in the manipulation of a single Bi atom, as is shown in Fig. 4.12. The used setpoint current was 12 nA and the bias voltage was 0.15 V. In this case, the trace of the tip height and tunnelling current shows a different behaviour. It start by showing the smooth movement of the tip hovering above the adatom, until a sudden jump in the tunnelling current occurs. This jump likely is the result of the atom hopping towards the tip, as was described above. After that, the tip-sample distance in steadily increased without altering the tunnelling current. This behaviour corresponds to that observed when the tip is in point contact (see Fig. 4.14), where the tunnelling current is invariant to changes in tip-sample distance. The sudden decrease in the tunnelling current that subsequently occurs, would correspond to the reverse of the jump observed in Fig. 4.14b.

These examples show that, in principle, lateral manipulation of adatoms is possible on Bi(111). This is confirmed by DFT calculations on the adsorption energy of a Bi atom on Bi(111). The adsorption energy was found to be −1.34 eV and the diffusion barrier between closed-packed rows was 0.26 eV. This adsorption energy is only half of that reported by ref. [60]. A different Bi coverage in the simulations might be able to be the reason for this: one adatom per 9 surface atoms here, opposed to one in 16 in [60]. Since the adsorption energy is about five times larger than the diffusion barrier, lateral manipulation in this direction should indeed be possible. However, lateral manipulation succeeded in less than 5 % of the attempts. Most frequently, the result of a lateral manipulation attempt was the transfer of the adsorbate from the surface to tip. Since this is the first step in the process of vertical manipulation, we switched our focus to this other mode for adsorbate displacement.

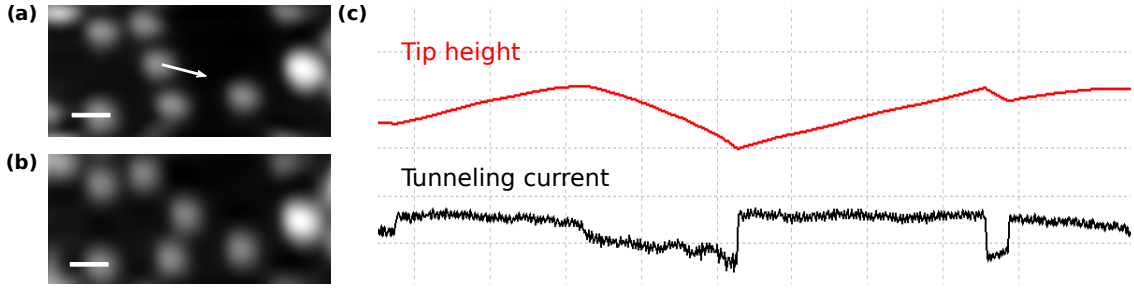

Figure 4.12: STM topographs before (a) and after (b) the lateral manipulation of the Bi atom, showing that the manipulation was successful. Scale bar are 1 nm. (c) Tip height and tunnelling current measured during the manipulation. Hopping of the atom is characterized by the step-like jump in tunnelling current, after which the tip is in point contact.

Vertical manipulation

As mentioned above, lateral manipulation attempts often resulted in the transfer of the adsorbate to the tip. An example of this is shown in Fig. 4.13. From the topographs taken before and after the manipulation (Fig. 4.13a, b), we know that the atom is picked up. Insight into how this occurred, can be obtained from the tip height trace (Fig. 4.13c). The tip starts by hovering over the adatom, until there is a sudden jump in the tunnelling current. Via the feedback loop, the tip height is adjusted such that the setpoint current is restored. The tip-sample distance required to reach the setpoint current is higher than before the jump, which is known to be a result of sample-to-tip transfer [17].

Another way to pick up an adsorbate would be to approach it vertically until it hops from the surface to the tip. We have tried to do this in two ways, which both use a constant bias voltage. In the first, we disabled the feedback loop and gradually approached the adsorbate with the tip. The second method consist of hovering above the adsorbate and gradually increasing the setpoint tunnelling current. The feedback loop was not disabled in this second method, which is actually the only difference between the two modes: in both, the STM tip approaches the adsorbate vertically. We did not expect this to affect the outcome, since the feedback loop operates on a much longer time scale than the adsorbate does. However, we had more success with the second method, in which the feedback loop was enabled. We have not been able to come up with a reasonable explanation for this.

For the combination of a Bi(111) surface and Bi or Pb adsorbates, the vertical manipulation mode might be a valid option for controlled adsorbate displacement, given that the adsorbates are

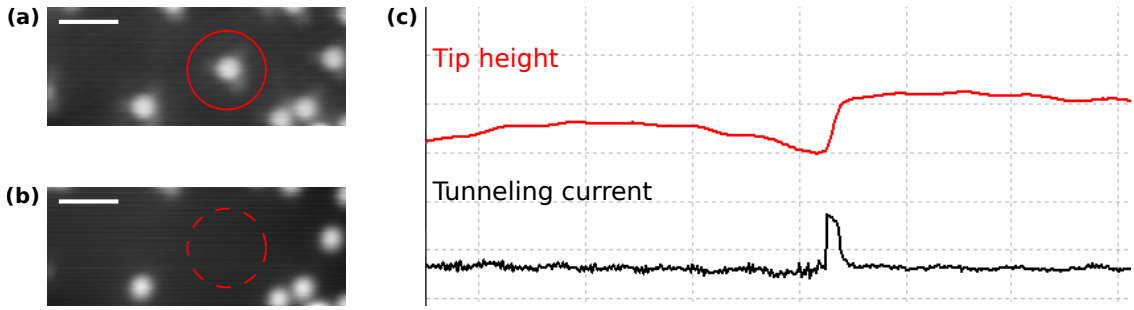

Figure 4.13: STM topographic image before (a) and after (b) the attempt at lateral manipulation, showing that the adatom is removed from the surface. Scale bars are 2 nm. (c) Trace of tip height (red, upper) and tunnelling current (black, lower) during the manipulation. The tip height curve initially follows the shape of the adatom, maintaining a constant tunnelling current. The sudden increase in the current, an indication for an event at the nanoscale, is quickly cancelled by the feedback loop.

relatively easily transferred to the tip. To transfer the adsorbates back onto the surface, we applied the strategy of Yang et al., who used vertical manipulation to position In atoms onto the InAs(111) surface [64]. Atoms were transferred to the surface by positioning the tip above the intended destination, switching to negative bias, before decreasing the tip-sample distance (feedback is disabled). The tip-to-surface transfer was characterized by a sudden jump in tunnelling current, after which the current remains nearly invariant with decreasing tip height (see Fig. 4.14a).

Attempts to achieve the same results on Bi(111) resulted in curves that are similar at first sight. From the current versus tip height curves in Fig. 4.14b, it can be observed that the tunnelling current gradually increases upon decreasing tip height, which is at a certain point followed by a jump in tunnelling current. After this jump, the tunnelling current is nearly constant. Up to this point, our results seem to match those of ref. [64]. However, the surface configuration did not change - no tip-to-surface transfer has occurred.

A closer comparison of our graphs to those presented by ref. [64] reveals that two are actually quite different. Firstly, the absolute scale of tunnelling current is very different. Where tunnelling currents in our case did not exceed 100 nA (at these voltages), several µAs were accomplished at the InAs surface. Secondly, the contribution of the jump to the final current is only minor for the Bi case: the total current increases with only 5-10 %. In contrast, an increase of one order of magnitude was observed on the InAs-surface.

The sudden jump in the tunnelling current is the result of the tip reaching mechanical contact with the surface, rather than the transfer of the atom. The conductance (I/V) at this point is much smaller than is to be expected for the situation of metallic point contact [65], which is ascribed to the longer Fermi wavelength in InAs or Sb, opposed to a simple metal [66]. The small size of the contact between surface and tip, compared to the Fermi wavelength, inhibits electrons to flow through this contact. Therefore, only tunnelling contributes to the measured current. This was confirmed by Yang et al., who showed that the voltage dependency of point contact conductance follows the rescaled tunnelling conductance at imaging settings [64]. However, this seems not to apply to Bi. Rescaling of the tunnelling conductance acquired at imaging settings (0.5 nA, 2.0 V) does not yield any reasonable results, unless a vertical shift is applied (see Fig. 4.14c). Point contact conductance increases by less than 10 % going from −0.5 V to −1.0 V in the case of Bi, whereas an increase of an order of magnitude is observed for InAs. Rescaling without applying a vertical shift to the data requires the tunnelling conductance data to be multiplied by a factor 1×10^5. The point contact conductance is then only matched at bias voltages close to 0 V (see Appendix C). By interpreting the results on this scale, it seems that point contact conductance seems to be independent of bias voltage. This is in contrast with the observations of ref. [64] and with the proposed explanation for the observed sub-quantum conductance mentioned above.

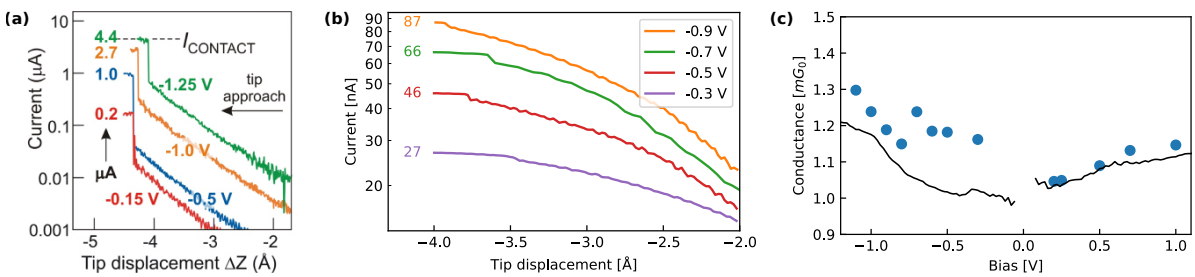

Figure 4.14: Tunnelling current versus tip displacement (from imaging height) on InAs(111)A (a) [64] and Bi(111) (b). On both surfaces, a jump can be observed corresponding to the tip reaching point contact. On the InAs(111)A surface, this is accompanied by tip-to-surface transfer of a single atom. (c) Measured conductance in point contact on Bi(111) at different voltages (blue circles) and rescaled and shifted tunnelling curve (black line). Conductance values are scaled a ratio of metallic point contact conductance G_0 (= $2e^2/h$).

The transfer of an atom at the tip-apex onto the surface can be explained by considering the forces allowing this process. When the tip-sample distance is sufficiently small, the surface atoms will interact with the atom at the tip apex. As soon as the atom-surface bond is stronger than the atom-tip interaction, the atom will be transferred to the surface. However, in our experiments there was either no transfer of anything, or transfer of a small structure of multiple atoms. The bond between the atom and the tip apex is thus too strong, compared to the bonds between other atoms in the tip apex. This could be due to the tendency of Bi to form bilayered structures. In the process of preparing a sharp tip, it is dipped into the Bi surface and we can thus assume that the tip apex is completely made up out of Bi atoms. The apex might then also consist of alternating strong and weak bonds, just as can be found in the bulk. When the forces originating from the surface are then pulling onto the tip apex, it can be expected to fracture at one of these weak bonds.

It could also be that heavy element adatoms, due to their covalent character, are more strongly bound to the tip apex than metallic atoms such as Cu or Ag. The surface forces acting on the atom at the tip apex are then simply not strong enough to establish the transfer of (part of) the tip apex onto the surface. This is supported by the observed ease with which atoms are transferred from surface to tip. Also the high polarizability of these heavy atoms, which increases the magnitude of the van der Waals forces acting on them, might play a role in this.

5 Conclusions

Si(111) surfaces were cleaned via the application of a well-known flashing procedure. This resulted in 7x7 reconstructed terraces with sizes up to 1 μm x 1 μm. Flat Bi(111) nanofilms were obtained by evaporation of elemental Bi and subsequently annealing at 130 °C for 6 h. Terraces with areas of 50 nm x 50 nm have been observed on films with a nominal thickness of 8-15 BL.

Investigation of the electronic properties of grown films, reproduced the results from literature concerning surface state energies and edge state energy. Surprisingly, DFT simulations of hydrogen-terminated Bi slabs allowed for a reasonable match to the experimental data concerning the surface state(s). It is not clear why simulations of freestanding slabs, as is common for Bi(111) on Si(111), yield a worse match.

Scattering of the surface state on adsorbates and crystal defects shows a threefold symmetric scattering pattern, as a result of the physical structure of the surface in real space and the Fermi surface in reciprocal space. Surface state electrons can be confined by adatoms, as is observed in a triangle formed by three Pb adatoms. Additionally, Pb atoms might allow for localization of surface state electrons with $E > E_F$.

CO molecules cannot be used as the scattering center for the Bi(111) surface state, since they cannot adsorb onto Bi(111). This is the result of repulsion between Bi atoms in the topmost layer and the CO molecules, as was reasoned through a molecular orbital picture. DFT calculations quantitatively confirmed this.

Although we did show that it is possible to manipulate Pb and Bi adatoms on Bi(111) with the STM tip, we have not found a reliable procedure to do so, yet. The adatoms tend to hop onto the tip, from where transfer back to the surface showed to be challenging. This impedes their application in both lateral and vertical manipulation modes. The covalent character and high polarizability of Pb and Bi atoms are suggested to be the reason for the observed problems.

6 Outlook

The work presented in this report has only been the very start of the investigation of Bi(111) for this purpose. As a result, many observations remain unexplained and further research could aid in solving these questions. For example, well-structured STS experiments could shed light on the behaviour of the surface state electrons in the proximity of adatoms. Of more importance for adatom manipulation would be to elucidate the interactions between tip, surface and adatoms. Structural variation of manipulation parameters will give more insight into the factors controlling the process. A better understanding of these factors could then help in finding a procedure for reliable displacement of adatoms.

If the manipulation of heavy element atoms proves to be too difficult to be used in the construction of artificial lattices, other scatterers can be considered. There are multiple options for alternative scatterers. Insight into the relevant interactions for the heavy element adatoms might influence the choice for the alternative. For example, period 4 transition metal atoms, such as Fe, Co or Cu, will be less influenced by van der Waals forces, because of their lower polarizability. It might also be that the interaction strength between adsorbate and surface is to be decreased. This might be accomplished by the use of Zn, which is calculated to bind only weakly to Bi(111) [60]. Alternatively, a small molecule might be used to this end. Care must than be taken that this molecule, in contrast to CO, is able to bind onto Bi(111). Additionally, the nature and shape of the molecule will influence its scattering properties.

As soon as a scatterer is found that can be reliably manipulated, quantum simulations on Bi(111) can, in principle, be performed. How artificial lattices should be constructed will then be the next question. Since the Bi(111) surface state cannot be considered as a (nearly-)free electron gas, confined electrons may behave differently than expected. Therefore, simulations of systems that are well-known and allow for easy interpretation should be performed before turning to more complicated examples. DFT calculations of the build lattice might be a very useful tool in this process. Such calculations will require quite some computational effort, due to the large system size. SIESTA might the best choice for these calculations, being designed for simulating up to thousands of atoms.

After simulating known systems, Bi(111) may be used to predict properties of less-understood ones. Herein, the Rashba effect and the low DOS close to E_F can be used to study the effect of Rasbha SOC on the electronic properties of artificial lattices with a high energy resolution.

In another set of experiments, we could try to introduce electron-electron interactions into the simulations, making use of the semimetallic nature of Bi. Experiments would then be performed in a setup as reported by ref. [67], in which the sample is equipped with gate electrodes. Via the gate electrodes, the electron density of the film can be decreased, resultantly weakening the ability of the material to screen electric charges. By controlling the the bias voltage set over the gate electrodes, electron-electron interactions can controllably be turned on and off. These simulation would allow for investigation of systems which cannot be described without Coulomb repulsions. Examples of such systems are conventional superconductors, which thank their excellent conductivity to electron-electron interactions.

Acknowledgements

Working on this project for the last one and a half years has been a real pleasure to me. It has allowed me to discover research on the boundary between chemistry and physics. However, I have not been alone on this voyage of discovery and therefore, I would like to thank some people.

To start, I would like to thank *Jesper* and *Thomas* for introducing me to the collection of stainless steel components that we refer to as the Gauss. Without the help of you two, I would have filled my time here with attempts at inserting samples into the TRIBUS. Next, I would like to thank *Ingmar*, first of all for giving me the opportunity to work on this project. Moreover, your help on theoretical problems and your practical advice have been very valuable. I would also like to acknowledge *Daniël* for his consultation and for keeping a watchful eye on the project. *Saoirsé*, thank you for allowing me to occupy one of your master students spots. For the help with getting to know SIESTA, I would like to thank *Pierre*. Lastly, I would like to thank *everyone in the CMI group*, especially the *members of Team Kelder* and the *master students*. The great atmosphere in the Ornstein laboratory you guys provided, allowed me to work on my thesis in the presence of an optimal combination of expertise, diversity and fun.

References

[1] Press release: The Nobel Prize in Chemistry 2016. https://www.nobelprize.org/prizes/chemistry/2016/press-release/.

[2] Press release: The Nobel Prize in Physics 2018. https://www.nobelprize.org/prizes/physics/2018/press-release/.

[3] Eigler, D. M.; Schweizer, E. K. Positioning single atoms with a scanning tunnelling microscope. *Nature* **1990**, *344*, 524–526, DOI: 10.1038/344524a0.

[4] Shockley, W. On the surface states associated with a periodic potential. *Physical Review* **1939**, *56*, 317–323, DOI: 10.1103/PhysRev.56.317.

[5] Crommie, M. F.; Lutz, C. P.; Eigler, D. M. Imaging standing waves in a two-dimensional electron gas. *Nature* **1993**, *363*, 524–527, DOI: 10.1038/363524a0.

[6] Crommie, M. F.; Lutz, C. P.; Eigler, D. M. Confinement of Electrons to Quantum Corrals on a Metal Surface. *Science* **1993**, *262*, 218–220, DOI: 10.1126/science.262.5131.218.

[7] Gomes, K. K.; Mar, W.; Ko, W.; Guinea, F.; Manoharan, H. C. Designer Dirac fermions and topological phases in molecular graphene. *Nature* **2012**, *483*, 306–310, DOI: 10.1038/nature10941.

[8] Slot, M. R.; Gardenier, T. S.; Jacobse, P. H.; Van Miert, G. C.; Kempkes, S. N.; Zevenhuizen, S. J.; Smith, C. M.; Vanmaekelbergh, D.; Swart, I. Experimental realization and characterization of an electronic Lieb lattice. *Nature Physics* **2017**, *13*, 672–676, DOI: 10.1038/nphys4105.

[9] Collins, L. C.; Witte, T. G.; Silverman, R.; Green, D. B.; Gomes, K. K. Imaging quasiperiodic electronic states in a synthetic Penrose tiling. *Nature Communications* **2017**, *8*, DOI: 10.1038/ncomms15961.

[10] Kempkes, S. N.; Slot, M. R.; Freeney, S. E.; Zevenhuizen, S. J. M.; Vanmaekelbergh, D.; Swart, I.; Smith, C. M. Design and characterization of electrons in a fractal geometry. *Nature Physics* **2018**, DOI: 10.1038/s41567-018-0328-0.

[11] Xiao, S.; Wei, D.; Jin, X. Bi(111) thin film with insulating interior but metallic surfaces. *Physical Review Letters* **2012**, *109*, DOI: 10.1103/PhysRevLett.109.166805.

[12] Voigtländer, B. *Scanning Probe Microscopy*; NanoScience and Technology; Springer Berlin Heidelberg: Berlin, Heidelberg, 2015; DOI: 10.1007/978-3-662-45240-0.

[13] Chen, C. J. *Introduction to Scanning Tunneling Microscopy: Second Edition*; Oxford University Press, 2007; Vol. 9780199211; pp 1–432, DOI: 10.1093/acprof:oso/9780199211500.001.0001.

[14] Hoffman, J. Scanning Tunneling Microscopy. 2013; http://hoffman.physics.harvard.edu/research/STMintro.php.

[15] Meyer, G.; Zöphel, S.; Rieder, K. H. Manipulation of atoms and molecules with a low temperature scanning tunneling microscope. *Applied Physics A Materials Science and Processing* **1996**, *63*, 557–564, DOI: 10.1007/BF01567211.

[16] Ruffieux, P.; Wang, S.; Yang, B.; Sánchez-Sánchez, C.; Liu, J.; Dienel, T.; Talirz, L.; Shinde, P.; Pignedoli, C. A.; Passerone, D.; Dumslaff, T.; Feng, X.; Müllen, K.; Fasel, R. On-surface

synthesis of graphene nanoribbons with zigzag edge topology. *Nature* **2016**, *531*, 489–492, DOI: 10.1038/nature17151.

[17] Eigler, D. M.; Lutz, C. P.; Rudge, W. E. An atomic switch realized with the scanning tunnelling microscope. *Nature* **1991**, *352*, 600–603, DOI: 10.1038/352600a0.

[18] Stroscio, J. A.; Eigler, D. M. Atomic and Molecular Manipulation with the Scanning Tunneling Microscope. *Science* **1991**, *254*, 1319–1326, DOI: 10.1126/science.254.5036.1319.

[19] Fiete, G. A.; Heller, E. J. Colloquium : Theory of quantum corrals and quantum mirages. *Reviews of Modern Physics* **2003**, *75*, 933–948, DOI: 10.1103/RevModPhys.75.933.

[20] Hasegawa, Y.; Avouris, P. Direct observation of standing wave formation at surface steps using scanning tunneling spectroscopy. *Physical Review Letters* **1993**, *71*, 1071–1074, DOI: 10.1103/PhysRevLett.71.1071.

[21] Kliewer, J. Dimensionality Effects in the Lifetime of Surface States. *Science* **2000**, *288*, 1399–1402, DOI: 10.1126/science.288.5470.1399.

[22] Hörmandinger, G.; Pendry, J. B. Interaction of surface states with rows of adsorbed atoms and other one-dimensional scatterers. *Physical Review B* **1994**, *50*, 18607–18620, DOI: 10.1103/PhysRevB.50.18607.

[23] Crampin, S.; Boon, M. H.; Inglesfield, J. E. Influence of Bulk States on Laterally Confined Surface State Electrons. *Physical Review Letters* **1994**, *73*, 1015–1018, DOI: 10.1103/PhysRevLett.73.1015.

[24] Ast, C. R.; Höchst, H. Fermi surface of bi(111) measured by photoemission spectroscopy. *Physical Review Letters* **2001**, *87*, 177602, DOI: 10.1103/PhysRevLett.87.177602.

[25] Du, H.; Sun, X.; Liu, X.; Wu, X.; Wang, J.; Tian, M.; Zhao, A.; Luo, Y.; Yang, J.; Wang, B.; Hou, J. G. Surface Landau levels and spin states in bismuth (111) ultrathin films. *Nature Communications* **2016**, *7*, 10814, DOI: 10.1038/ncomms10814.

[26] Bian, G.; Wang, X.; Kowalczyk, P. J.; Maerkl, T.; Brown, S. A.; Chiang, T. C. Survey of electronic structure of Bi and Sb thin films by first-principles calculations and photoemission measurements. *Journal of Physics and Chemistry of Solids* **2017**, DOI: 10.1016/j.jpcs.2017.07.027.

[27] Hofmann, P. The surfaces of bismuth: Structural and electronic properties. *Progress in Surface Science* **2006**, *81*, 191–245, DOI: 10.1016/j.progsurf.2006.03.001.

[28] Drozdov, I. K.; Alexandradinata, A.; Jeon, S.; Nadj-Perge, S.; Ji, H.; Cava, R. J.; Bernevig, B. A.; Yazdani, A. One-dimensional topological edge states of bismuth bilayers. *Nature Physics* **2014**, *10*, 664–669, DOI: 10.1038/nphys3048.

[29] Nagao, T.; Yaginuma, S.; Saito, M.; Kogure, T.; Sadowski, J. T.; Ohno, T.; Hasegawa, S.; Sakurai, T. Strong lateral growth and crystallization via two-dimensional allotropic transformation of semi-metal Bi film. *Surface Science* **2005**, *590*, 247–252, DOI: 10.1016/j.susc.2005.06.004.

[30] Bychkow, Y. A.; Rashba, E. I. Properties of a 2D electron gas with lifted spin degeneracy. *JETP Lett.* **1984**, *39*, 66–69.

[31] Hirahara, T.; Nagao, T.; Matsuda, I.; Bihlmayer, G.; Chulkov, E. V.; Koroteev, Y. M.; Echenique, P. M.; Saito, M.; Hasegawa, S. Role of spin-orbit coupling and hybridization effects in the electronic structure of ultrathin Bi films. *Physical Review Letters* **2006**, *97*, 10–13, DOI: 10.1103/PhysRevLett.97.146803.

[32] Nečas, D.; Klapetek, P. Gwyddion: an open-source software for SPM data analysis. *Open Physics* **2012**, *10*, DOI: 10.2478/s11534-011-0096-2.

[33] Soler, J. M.; Artacho, E.; Gale, J. D.; García, A.; Junquera, J.; Ordejón, P.; Sánchez-Portal, D. The SIESTA method for ab initio order- N materials simulation. *Journal of Physics: Condensed Matter* **2002**, *14*, 2745–2779, DOI: 10.1088/0953-8984/14/11/302.

[34] Perdew, J. P.; Burke, K.; Ernzerhof, M. Generalized Gradient Approximation Made Simple. *Physical Review Letters* **1996**, *77*, 3865–3868, DOI: 10.1103/PhysRevLett.77.3865.

[35] Cuadrado, R.; Cerdá, J. I. Fully relativistic pseudopotential formalism under an atomic orbital basis: spin–orbit splittings and magnetic anisotropies. *Journal of Physics: Condensed Matter* **2012**, *24*, 086005, DOI: 10.1088/0953-8984/24/8/086005.

[36] Junquera, J.; Paz, Ó.; Sánchez-Portal, D.; Artacho, E. Numerical atomic orbitals for linear-scaling calculations. *Physical Review B* **2001**, *64*, 235111, DOI: 10.1103/PhysRevB.64.235111.

[37] van Setten, M. J.; Giantomassi, M.; Bousquet, E.; Verstraete, M. J.; Hamann, D. R.; Gonze, X.; Rignanese, G. M. The PSEUDODOJO: Training and grading a 85 element optimized norm-conserving pseudopotential table. *Computer Physics Communications* **2018**, *226*, 39–54, DOI: 10.1016/j.cpc.2018.01.012.

[38] Monkhorst, H. J.; Pack, J. D. Special points for Brillouin-zone integrations. *Physical Review B* **1976**, *13*, 5188–5192, DOI: 10.1103/PhysRevB.13.5188.

[39] Jupnik, H. Photoelectric Properties of Bismuth. *Physical Review* **1941**, *60*, 884–889, DOI: 10.1103/PhysRev.60.884.

[40] Liu, Y.; Allen, R. E. Electronic structure of the semimetals Bi and Sb. *Physical Review B* **1995**, *52*, 1566–1577, DOI: 10.1103/PhysRevB.52.1566.

[41] Bengtsson, L. Dipole correction for surface supercell calculations. *Physical Review B* **1999**, *59*, 12301–12304, DOI: 10.1103/PhysRevB.59.12301.

[42] Papior, N. sisl: tight-binding and DFT interface library. 2019; https://doi.org/10.5281/zenodo.597181.

[43] Takayama, A.; Sato, T.; Souma, S.; Oguchi, T.; Takahashi, T. Tunable spin polarization in bismuth ultrathin film on Si(111). *Nano Letters* **2012**, *12*, 1776–1779, DOI: 10.1021/nl2035018.

[44] Matetskiy, A. V.; Bondarenko, L. V.; Tupchaya, A. Y.; Gruznev, D. V.; Eremeev, S. V.; Zotov, A. V.; Saranin, A. A. Adsorbate-induced modification of electronic band structure of epitaxial Bi(111) films. *Applied Surface Science* **2017**, *406*, 122–127, DOI: 10.1016/j.apsusc.2017.02.023.

[45] Payer, T.; Klein, C.; Acet, M.; Ney, V.; Kammler, M.; Meyer Zu Heringdorf, F. J.; Horn-Von Hoegen, M. High-quality epitaxial Bi(111) films on Si(111) by isochronal annealing. *Thin Solid Films* **2012**, *520*, 6905–6908, DOI: 10.1016/j.tsf.2012.06.004.

[46] Kawakami, N.; Lin, C. L.; Kawai, M.; Arafune, R.; Takagi, N. One-dimensional edge state of Bi thin film grown on Si(111). *Applied Physics Letters* **2015**, *107*, 031602, DOI: 10.1063/1.4927206.

[47] Takayama, A.; Sato, T.; Souma, S.; Oguchi, T.; Takahashi, T. One-Dimensional Edge States with Giant Spin Splitting in a Bismuth Thin Film. *Physical Review Letters* **2015**, *114*, 066402, DOI: 10.1103/PhysRevLett.114.066402.

[48] Yaginuma, S.; Nagao, T.; Sadowski, J. T.; Saito, M.; Nagaoka, K.; Fujikawa, Y.; Sakurai, T.; Nakayama, T. Origin of flat morphology and high crystallinity of ultrathin bismuth films. *Surface Science* **2007**, *601*, 3593–3600, DOI: 10.1016/j.susc.2007.06.075.

[49] Nagao, T.; Sadowski, J. T.; Saito, M.; Yaginuma, S.; Fujikawa, Y.; Kogure, T.; Ohno, T.; Hasegawa, Y.; Hasegawa, S.; Sakurai, T. Nanofilm allotrope and phase transformation of ultrathin Bi film on Si(111)-7×7. *Physical Review Letters* **2004**, *93*, 105501, DOI: 10.1103/PhysRevLett.93.105501.

[50] Yaginuma, S.; Nagao, T.; Sadowski, J. T.; Pucci, A.; Fujikawa, Y.; Sakurai, T. Surface pre-melting and surface flattening of Bi nanofilms on Si(1 1 1)-7 × 7. *Surface Science* **2003**, *547*, L877–L881, DOI: 10.1016/j.susc.2003.10.015.

[51] Koroteev, Y. M.; Bihlmayer, G.; Chulkov, E. V.; Blügel, S. First-principles investigation of structural and electronic properties of ultrathin Bi films. 2008; https://link.aps.org/doi/10.1103/PhysRevB.77.045428.

[52] Cantele, G.; Ninno, D. Size-dependent structural and electronic properties of Bi(111) ultrathin nanofilms from first principles. *Physical Review Materials* **2017**, *1*, 014002, DOI: 10.1103/PhysRevMaterials.1.014002.

[53] Ito, S. et al. Proving Nontrivial Topology of Pure Bismuth by Quantum Confinement. *Physical Review Letters* **2016**, *117*, 236402, DOI: 10.1103/PhysRevLett.117.236402.

[54] Steinbrecher, M.; Harutyunyan, H.; Ast, C. R.; Wegner, D. Rashba-type spin splitting from interband scattering in quasiparticle interference maps. *Physical Review B* **2013**, *87*, 245436, DOI: 10.1103/PhysRevB.87.245436.

[55] Peng, L.; Xian, J.-J.; Tang, P.; Rubio, A.; Zhang, S.-C.; Zhang, W.; Fu, Y.-S. Visualizing topological edge states of single and double bilayer Bi supported on multibilayer Bi(111) films. *Physical Review B* **2018**, *98*, 245108, DOI: 10.1103/PhysRevB.98.245108.

[56] Cottin, M. C.; Bobisch, C. A.; Schaffert, J.; Jnawali, G.; Sonntag, A.; Bihlmayer, G.; Möller, R. Anisotropic scattering of surface state electrons at a point defect on Bi(111). *Applied Physics Letters* **2011**, *98*, 022108, DOI: 10.1063/1.3536528.

[57] Olsson, F. E.; Persson, M.; Borisov, A. G.; Gauyacq, J.-P.; Lagoute, J.; Fölsch, S. Localization of the Cu(111) Surface State by Single Cu Adatoms. *Physical Review Letters* **2004**, *93*, 206803, DOI: 10.1103/PhysRevLett.93.206803.

[58] Gauyacq, J. P.; Borisov, A. G.; Kazansky, A. K. Impurity-induced localisation of the 2D surface-state continuum on a metal surface. *Applied Physics A: Materials Science and Processing* **2004**, *78*, 141–147, DOI: 10.1007/s00339-003-2299-x.

[59] Zaum, C.; Morgenstern, K. Voltage dependent STM imaging of inorganic adsorbates. *Applied Physics Letters* **2018**, *113*, 031602, DOI: 10.1063/1.5032174.

[60] Klein, C.; Vollmers, N. J.; Gerstmann, U.; Zahl, P.; Lükermann, D.; Jnawali, G.; Pfnür, H.; Tegenkamp, C.; Sutter, P.; Schmidt, W. G.; Horn-Von Hoegen, M. Barrier-free subsurface incorporation of 3d metal atoms into Bi(111) films. *Physical Review B - Condensed Matter and Materials Physics* **2015**, *91*, 195441, DOI: 10.1103/PhysRevB.91.195441.

[61] Hollins, P.; Pritchard, J. Interactions of CO molecules adsorbed on Cu(111). *Surface Science* **1979**, *89*, 486–495, DOI: 10.1016/0039-6028(79)90633-2.

[62] Lovas, F. J.; Tiemann, E. Diatomic Spectra Database. 2005; https://www.nist.gov/pml/diatomic-spectral-database.

[63] Bartels, L.; Meyer, G.; Rieder, K.-H. Basic Steps of Lateral Manipulation of Single Atoms and Diatomic Clusters with a Scanning Tunneling Microscope Tip. *Physical Review Letters* **1997**, *79*, 697–700, DOI: 10.1103/PhysRevLett.79.697.

[64] Yang, J.; Nacci, C.; Martínez-Blanco, J.; Kanisawa, K.; Fölsch, S. Vertical manipulation of native adatoms on the InAs(111)A surface. *Journal of Physics: Condensed Matter* **2012**, *24*, 354008, DOI: 10.1088/0953-8984/24/35/354008.

[65] Limot, L.; Kröger, J.; Berndt, R.; Garcia-Lekue, A.; Hofer, W. A. Atom Transfer and Single-Adatom Contacts. *Physical Review Letters* **2005**, *94*, 126102, DOI: 10.1103/PhysRevLett.94.126102.

[66] Krans, J. M.; van Ruitenbeek, J. M. Subquantum conductance steps in atom-sized contacts of the semimetal Sb. *Physical Review B* **1994**, *50*, 17659–17661, DOI: 10.1103/PhysRevB.50.17659.

[67] Zhang, Y.; Brar, V. W.; Wang, F.; Girit, C.; Yayon, Y.; Panlasigui, M.; Zettl, A.; Crommie, M. F. Giant phonon-induced conductance in scanning tunnelling spectroscopy of gate-tunable graphene. *Nature Physics* **2008**, *4*, 627–630, DOI: 10.1038/nphys1022.

Appendices

A. System specific parameters

Listed below are some parameters, specific STM setup, used in the process of obtaining flat Bi(111) films.

Process	Method	Settings
Si wafer to 600 °C	Resistive heating plate	16 V, 3 A
Si wafer to 900 °C	DC current	1.9 A, 15 V
Si wafer to 1200 °C	DC current	6 A, 15 V
Bi evaporation at ca. 0.4 ML/ min	E-beam evaporation	22 nA
Bi annealing at 130 °C	Resistive heating plate	3.8 V, 2 A
Bi/Pb evaporation (sub-ML coverage)	E-beam evaporation	17-19 nA, 10 s

Table A.1: STM setup specific parameters for different steps in the preparation of the supported Bi(111) nanofilms.

B. Example of SIESTA input file

Provided is the SIESTA input file used for the calculation of the electronic properties of a relaxed slab of 10 BL, terminated with hydrogen atoms. For a detailed explanation of used parameters, the reader is referred to the SIESTA manual.

```
# System description
SystemLabel   10BL_elec_H
SystemName   Calculation on a 10 BL thick slab to compare with literature.

# Defining of the input structure
NumberOfSpecies   2
NumberOfAtoms   21
%block ChemicalSpecieslabel
     1 83 Bi_pseudodojo.1
     2 1 H.gga.2
%endblock ChemicalSpecieslabel

# Defines basis set
%block PAO.Basis
Bi_pseudodojo.1 3
n=6    0    2 S 0.4
 6.0    0.0
 1.0 1.0
n=6    1    2 P 1 E 40 -0.8   0.4
 9.0    0.0
 1.0 1.0
n=5    2    1
 3.8
 1.0
H.gga.2 1
```

```
n=1 0   2   S 0.1 P 2
 0.0 0.0
 1.0 1.0
%endblock PAO.Basis

# Defines unit cell
LatticeConstant  1.0 Ang
%block LatticeVectors
    4.545999557945527      0.000000000000000      0.000000000000000
    -2.272999779237352     3.936951103093932      0.000000000000000
    0.000000000000000      -0.000000000000000     57.202380301809633
%endblock LatticeVectors

# Defines coordinates of atoms
AtomicCoordinatesFormat  Ang
%block AtomicCoordinatesAndAtomicSpecies
     0.005694729      0.004010603      11.662334073 1
     2.278180401      1.316097130      10.021951479 1
     2.280375191      1.317909730      15.801861591 1
     0.006218081      2.629633827      14.161809672 1
     0.007256404      2.631257398      19.925895973 1
    -2.267814620      3.942446179      18.286138690 1
     0.005866892      0.007060740      24.027527224 1
     2.276013866      1.317800796      22.389799589 1
     2.275110355      1.317007362      28.124599592 1
    -0.001141267      2.627525833      26.486095928 1
    -0.001850548      2.627602262      32.224867920 1
    -0.005040363      0.001083046      30.586375709 1
    -0.006422094      0.001381053      36.321118759 1
     2.263732476      1.312065499      34.683388749 1
     2.265232815      1.311795681      40.424993070 1
    -0.009794167      2.622872098      38.785211936 1
    -0.007882749      2.623092198      44.549783587 1
    -2.281993436      3.934716711      42.909680354 1
    -0.006580764     -0.001081100      48.689610465 1
     2.265980543      1.310885746      47.049237616 1
     2.278180401      1.316097130       8.021951479 2
%endblock AtomicCoordinatesAndAtomicSpecies

# Defines computational details
PAO.EnergyShift  0.04000000 eV
%block PS.lmax
        Bi_pseudodojo.1 2
        H.gga.2 1
%endblock PS.lmax
XC.functional  GGA
XC.authors  PBE
Spin  spin-orbit
MaxSCFIterations  600
SCFMustConverge  true
DM.MixingWeight  0.05
DM.NumberPulay  8
SCF.Mixer.Restart  25
SCF.Mixer.Restart.Save  3
SCF.Mixer.Kick  10
SCF.Mixer.Kick.Weight  0.05
SCF.H.Tolerance  0.00001000 eV
DM.Tolerance  1e-05
```

```
MeshCutoff   5442.2772 eV
ElectronicTemperature   0.00035000 eV

%block kgrid_Monkhorst_Pack
      11        0        0   0.0
      0        11        0   0.0
      0        0        1   0.0
%endblock kgrid_Monkhorst_Pack
```

C. Point contact conductance without vertical shift

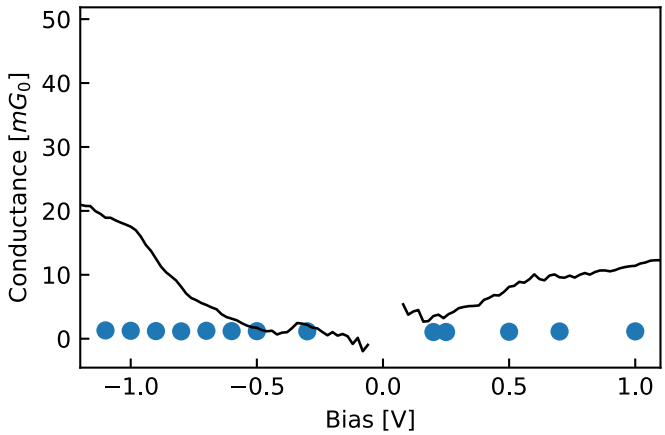

Figure C.1: Measured conductance in point contact on Bi(111) at different voltages (blue circles) and tunnelling curve, rescaled by 1×10^5 (black line). Conductance values are scaled a ratio of metallic point contact conductance G_0 ($= 2e^2/h$).